ACS OMEGA
http://pubs.acs.org/journal/acsodf
Article

Pore Structures and Evolution Model of Reservoirs in Different Secondary Structural Zones in the Eocene Shahejie Formation, Chezhen Sag, Bohai Bay Basin

Jinlei Xiu, Yang Li,* Yaohui Xu, Yan Liu,* and Zhanghu Wang

Cite This: ACS Omega 2024, 9, 22952–22969
Read Online

ACCESS | Metrics & More | Article Recommendations

ABSTRACT: Although abundant unconventional oil resources have been discovered in conglomerate and sandstone reservoirs in rift basins, the mechanism of differential pore evolution in conglomerates and sandstone reservoirs within different secondary structural zones of rift basins is not yet clear. The pore structures of conglomerate and sandstone reservoirs in the distinct secondary structural zones in the Chezhen Sag were quantified in three dimensions using high-resolution microcomputed tomography (micro-CT). Thin section and scanning electron microscopy observations were used to investigate the differential evolution mechanisms of conglomerate and sandstone reservoirs. Micro-CT analysis of the pore structures of conglomerate and sandstone reservoirs revealed that sandstone reservoirs are superior to conglomerate reservoirs with regard to the pore number and pore connectivity and that sandstone reservoirs are more heterogeneous than conglomerate reservoirs. Triangles dominate the pore and pore throat geometries of sandstone and conglomerate reservoirs, while the sandstone reservoir pores are more regular than conglomerate reservoir pores. The depositional environment, mineral composition, and diagenetic intensity jointly control the quality of the reservoirs. Because of the lengthy transportation distance of their parent rocks, the compositional maturity and sorting behavior of sandstone reservoirs in depression and gentle slope zones are better than those of conglomerate reservoirs in steep slope zones, and thus sandstone reservoirs have a higher initial porosity than conglomerate reservoirs. The rapid compaction experienced by the conglomerate reservoirs in steep slope zones in their early stages creates a closed diagenetic environment, making it difficult to effectively improve reservoir porosity through dissolution. However, the widely developed microfractures in the reservoirs provide channels for fluid migration, promote the development of dissolution pores, and form a tight reservoir dominated by secondary pores. With weak compaction and an open diagenetic environment, the primary pores in sandstone reservoirs in the gentle slope zone are preserved in large quantities. Meanwhile, dissolution expands the secondary pores of the reservoir, resulting in a high-quality reservoir having both primary and secondary pores. In addition, an approach based on primary, secondary, and total porosity was proposed in the study to efficiently evaluate reservoir quality and identify reservoir evolution mechanisms.

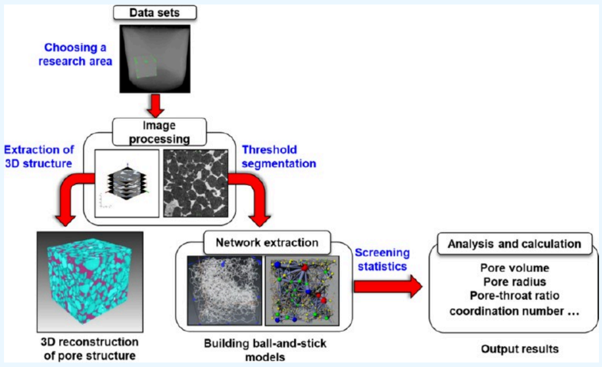

1. INTRODUCTION

Great strides have been made in the study of reservoir internal structures owing to the development of characterization technologies for oil- and gas-bearing reservoirs. The micropore structure of these reservoirs is critical for the migration and accumulation of water, gas, and crude oil and for the storage of carbon dioxide.[1−4] Geologists and engineers can accurately forecast oil sweet spots and increase their recovery rate by understanding the micropore structures of oil and gas reservoirs.[5] Therefore, to determine the relationship between the properties of the reservoirs and hydrocarbon migration and accumulation, the quantitative evaluation of the reservoir pore structure is necessary.[6,7] Because of their convoluted pore networks, tiny pore radius, poor connectivity, and heterogeneity, the micropore structures of tight reservoirs have long been a hot and challenging topic for researchers.[8,9]

The analysis of reservoir micropore structures through the application of high-pressure mercury injection, constant-rate mercury injection, nuclear magnetic resonance, and micro-CT is a transition from the qualitative description to quantitative characterization of the micropore structures.[10−18] The reservoir pore structures have shifted from being depicted in

Received: March 4, 2024
Revised: April 28, 2024
Accepted: May 7, 2024
Published: May 14, 2024

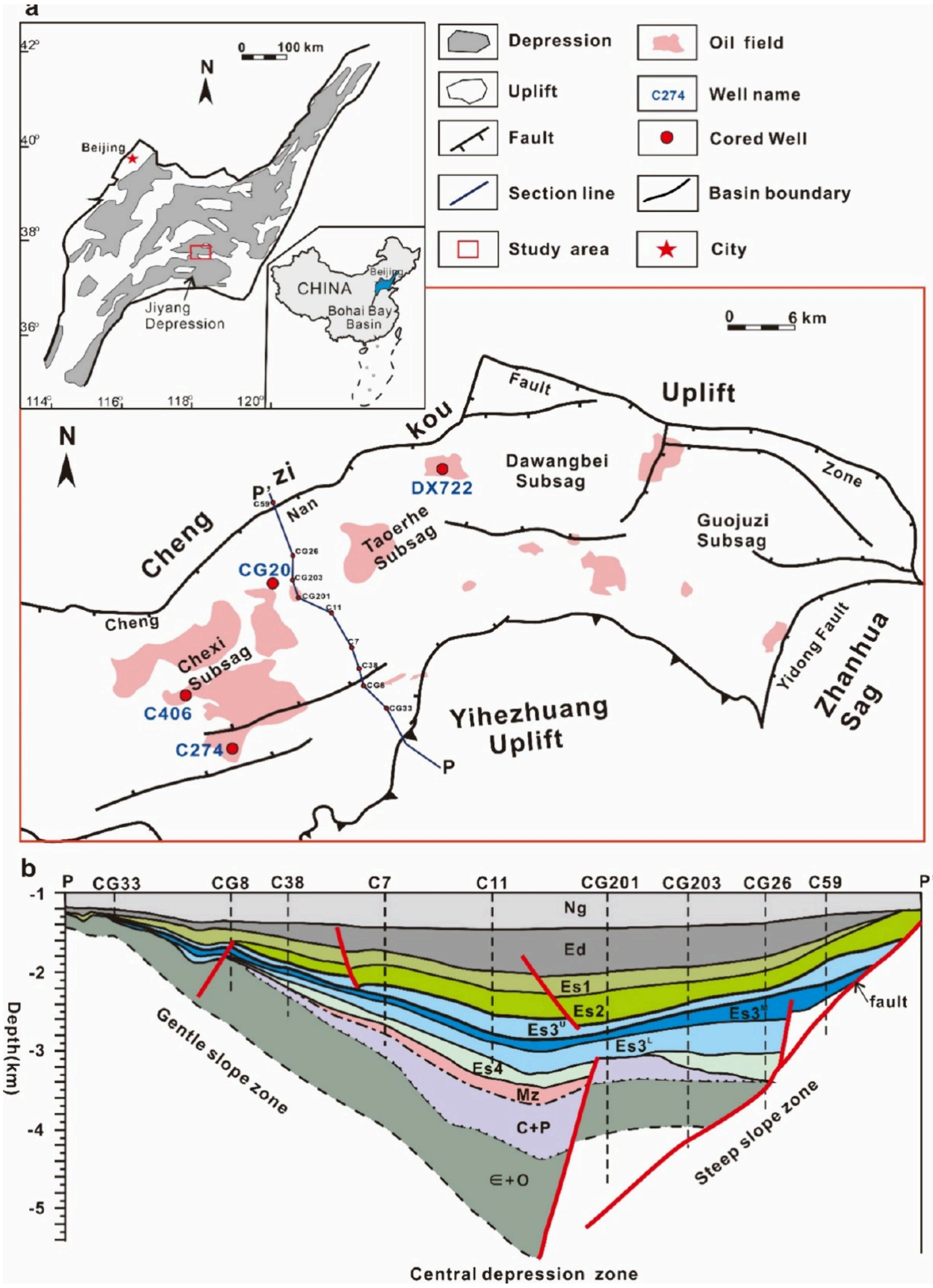

Figure 1. (a) Structural units and sampling well locations of the Chezhen Sag in the Bohai Bay Basin, China. (b) Distribution of the secondary structural zones of the Chezhen Sag (cross section presented in Figure 1(a)).

two dimensions to being characterized in three dimensions using X-ray micro-CT.[19−25] In addition, information on pore throat radius, pore numbers, and pore throat coordination numbers can be collected simultaneously using X-ray micro-CT.[7,26,27]

Micro(Nano)-CT is extensively used to evaluate the micropore structures of carbonate rock, tight sandstone, shale, and coal.[16,18,21,28−32] Only limited research has been conducted on the quantitative characterization of the micropore structures of tight conglomerate reservoirs in three dimensions. Conglomerate reservoirs in rift basins, however, contain abundant oil and gas resources according to the findings of recent explorations.[33−37] Several 100-million-ton conglomerate oilfields have been discovered in several parts of China, including the Chezhen Sag and Dongying Sag in the Bohai Bay Basin and Mahu Sag in the Junggar Basin.[38−42] Therefore, it is crucial to quantitatively quantify the micropore structures of conglomerate reservoirs and investigate their pore evolution mechanism. The large particle size of conglomerate reservoirs restricts the use of micro-CT for characterizing their micropore structures. Nevertheless, by selecting samples with appropriate diameters and using micro-CT analysis, thin section identification, and scanning electron microscopy (SEM) observations, the pore structure of a conglomerate reservoir can still be assessed quantitatively and accurately.

In this study, conglomerate and sandstone reservoirs in the Chezhen Sag were investigated. High-resolution micro-CT analysis, thin section identification, and SEM analysis, the pore structures of conglomerate and sandstone reservoirs in the separate secondary structural zones of faulted basins were

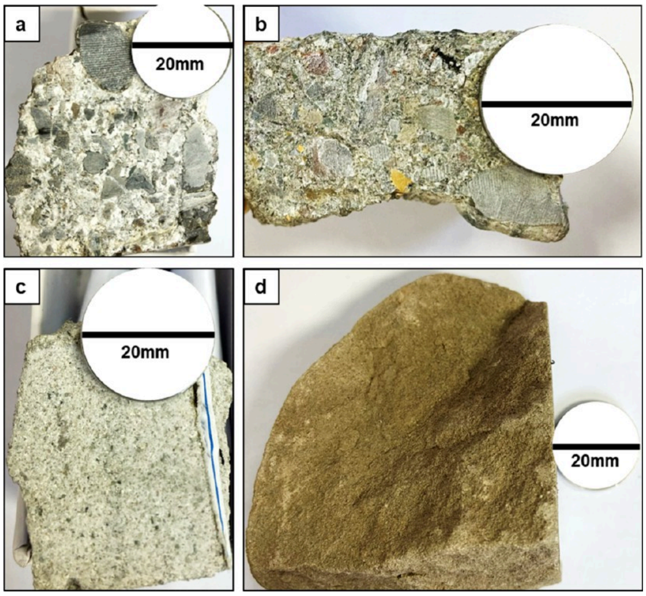

Figure 2. Photographs of the selected cores. (a) Conglomerate reservoir in Well CG20 in the steep slope zone. (b) Conglomerate reservoir in Well DX722 in the steep slope zone. (c) Sandstone reservoir in Well C406 in the depression zone. (d) Sandstone reservoir in Well C274 in the gentle slope zone.

quantitatively determined. The differential evolution mechanisms of reservoirs in different secondary structural zones of Chezhen Sag were also investigated. In addition, a clastic reservoir categorization scheme, which may reflect the controlling variables of reservoir quality and provide an effective theoretical foundation for predicting high-quality reservoirs, based on primary and secondary porosities was developed.

2. GEOLOGICAL BACKGROUND

The Chezhen Sag is located in the north of the Jiyang depression, southeast of the Bohai Bay Basin, Eastern China (Figure 1a). It is connected with the Chengzikou Uplift in the north, adjacent to the Zhanhua Sag, with the Yidong Fault in the east, and bounded to the south by the Yihezhuang Uplift (Figure 1a). The Chezhen Sag is separated into Chexi,

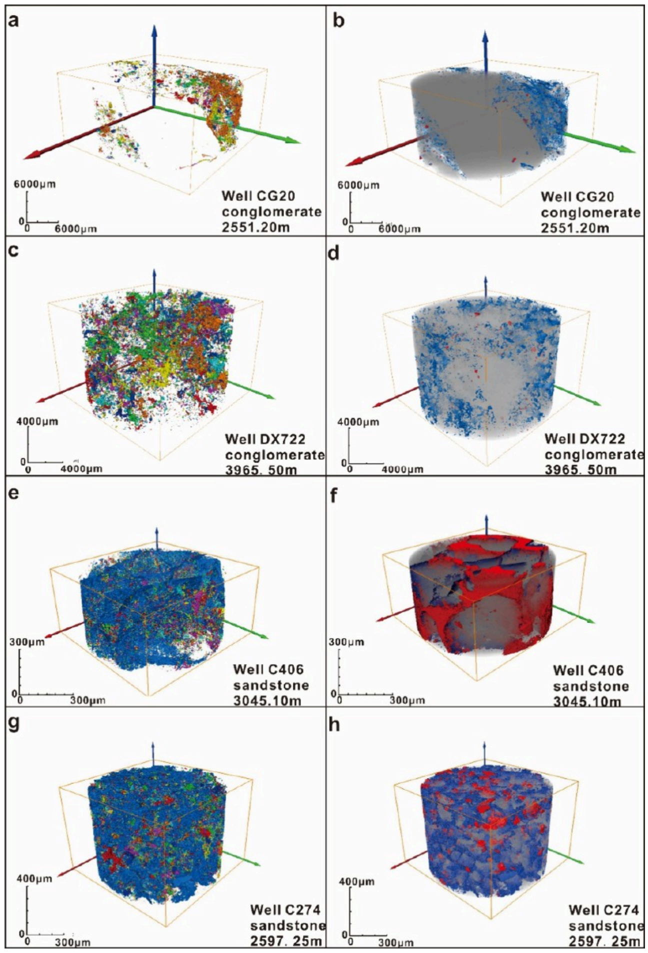

Figure 4. Three-dimensional characterization of the pore structures of conglomerate and sandstone reservoirs in the Chezhen Sag. The unconnected pores in (a), (c), (e), and (g) are identified by distinct colors, and in (b), (d), (f), and (h), blue indicates pores; gray represents particles; and red represents cements.

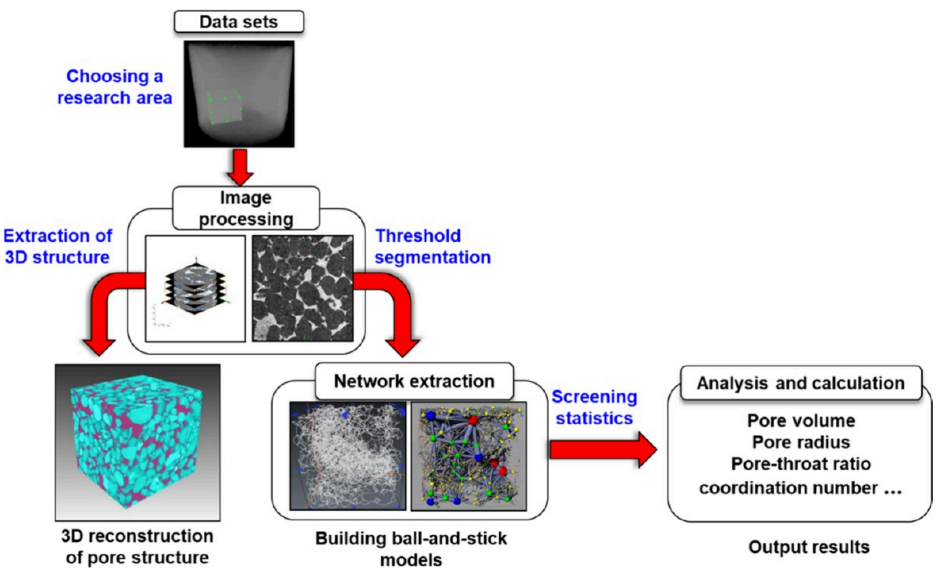

Figure 3. Flowchart of the digital core analysis performed using 3D imaging information provided by high-resolution microcomputed tomography.

Table 1. Quantitative Characterization Data of Pore Structures Based on High-Resolution Micro-Computed Tomography Digital Core Analysis

Parameters		CG20	DX722	C406	C274
Volume proportion	Pores (%)	0.21	1.49	7	7.15
	Cements (%)	0.01	0.05	17.53	4.87
	Detrital grains and matrix (%)	99.78	98.46	75.47	87.98
Size of pores and pore throats	Maximum pore radius (μm)	115.26	253.75	8.55	3.03
	Average pore radius (μm)	34.31	27.71	1.36	1.38
	Maximum pore−throat radius (μm)	86.56	116.30	4.61	2.28
	Average pore−throat radius (μm)	16.27	14.38	0.85	0.70
	Maximum pore−throat length (μm)	218.91	296.79	24.92	64.33
	Average pore−throat length (μm)	72.55	48.47	2.96	4.71
	Maximum pore−throat ratio	14.72	39.90	30.31	16.54
	Average pore−throat ratio	1.92	2.23	2.03	2.05
Pore volume	Maximum pore volume (μm^3)	8.64×10^7	6.31×10^8	38462.30	14887.50
	Average pore volume (μm^3)	4.86×10^6	1.98×10^6	231.12	834.80
	Maximum pore throat volume (μm^3)	2.76×10^7	2.61×10^7	2182.61	35271.00
	Average pore throat volume (μm^3)	1.52×10^6	3.31×10^5	11.80	115.14
Coordination number	Maximum coordination number	12	37	38	33
	Average coordination number	1	1	3	8

Taoerhe, Dawangbei, and Guojuzi Subsags along the east−west direction. Three distinct secondary structural zones run in the north−south direction: steep slope, central depression, and gentle slope zones (Figure 1(b)).

3. SAMPLES AND METHODS

3.1. Sample Selection and Preparation. The conglomerates come from Well CG20 in the steep slope zone of the Chexi Subsag and Well DX722 in the Dawangbei Subsag. The sandstones are extracted from Well C406 in the central depression zone of the Chexi Subsag and Well C274 in the gentle slope zone (Figure 1(b)). In addition to comparing the properties of conglomerate and sandstone reservoirs, the sample scheme described above can compare the properties of reservoirs in various secondary structural zones. The cross-sectional images of the core samples are shown in Figure 2. Before drilling the core samples for micro-CT analysis, they were oil-washed and dried. The drilled conglomerate samples had diameters between 20 and 30 mm, and thus they could represent a wide range of reservoir properties. To obtain a high-resolution photograph of the reservoir microstructure, the diameter of the drilled sandstone sample was set between 1 and 2 mm. The thickness of conglomerate and sandstone samples is 25 mm and 2 mm, respectively.

3.2. Experimental Conditions and Procedures. A nanoVoxel-3502E micro-CT scanner was used to obtain core sample images. In anticipation of beam hardening, a 0.20 mm thick copper beam filter was incorporated into the micro-CT scanner. The beam was exposed for 1,500 ms, and the scan took about 2 to 4 h. The conglomerate samples were scanned at a voltage of 150 kV, a current between 60 and 150 μA, and a resolution of 12 μm, whereas the sandstone samples were scanned at a voltage of 60 kV, a current between 30 and 50 μA, and a resolution of 0.61 μm. For each sample, 900−1,200 tomograms were imaged. A local means filter was applied to the grayscale images that were collected to reduce noise.[17] Avizo software effectively eliminated artifacts, such as rings and stiffenings, and the iterative reconstruction technique in the software reconstructed the images using low-dose scanning data. Then, using the widely used Otsu's algorithm, image segmentation was performed.[43] Using Avizo, the pore network was recovered from segmented three-dimensional (3D) data sets. Micro-CT scans were used to create 3D models of reservoir pore networks including the spatial configurations of their pores and throats. To measure the number of pores and throats, pore statistics were derived from image data using ball and stick models. Finally, the pore and pore throat sizes and pore volume fractions were quantified using 3D visualization. The experimental procedure described above is summarized in Figure 3. The thin sections were impregnated with blue epoxy under vacuum and stained with Alizarin red-S and potassium ferricyanide to examine mineral compositions, particle size analysis, and surface porosity statistics.[41] The scanning electron microscope (SEM) equipped with an EMAX-350 energy dispersive spectrometer were used to examine clay minerals. An acceleration voltage of 20 kV with an emission current of 10−12 μA, and a work distance range from 14.0 to 22.0 mm were the operating conditions.[41]

4. RESULTS

4.1. Three-Dimensional Reconstruction of the Pore Structures. In two-dimensional tomograms, the gray value of the pores remains low, while the gray value of clastic particles and cements gradually increase. Therefore, pores in a reservoir can be identified from the minerals in it. The porosity of each tomogram can be retrieved using threshold segmentation, which can acquire the porosity distribution along the Z-axis layer-wise and reconstruct the 3D pore distribution model. The extracted isolated pores are marked using different colors, and the pores of different sizes can be screened and counted by building ball and stick models. Numerous isolated pores are present in the conglomerate reservoirs in the steep slope zone of Chexi Subsag (Figure 4(a)). The massive detrital components (gray in color and accounting for 99.78% of the total volume) occupy almost the entire reservoir space, while the cements (red in color and accounting for 0.01% of the total volume) and pores (blue in color and accounting for 0.21% of the total volume) are scarcely developed (Figure 4(b) and Table 1). The conglomerate reservoir in the steep slope zone of Dawangbei Subsag has many isolated pores (Figure 4(c)). Detrital grains and interstitials continue to occupy most of the reservoir space (accounting for 98.46% of the total volume)

https://doi.org/10.1021/acsomega.4c02106
ACS Omega 2024, 9, 22952−22969

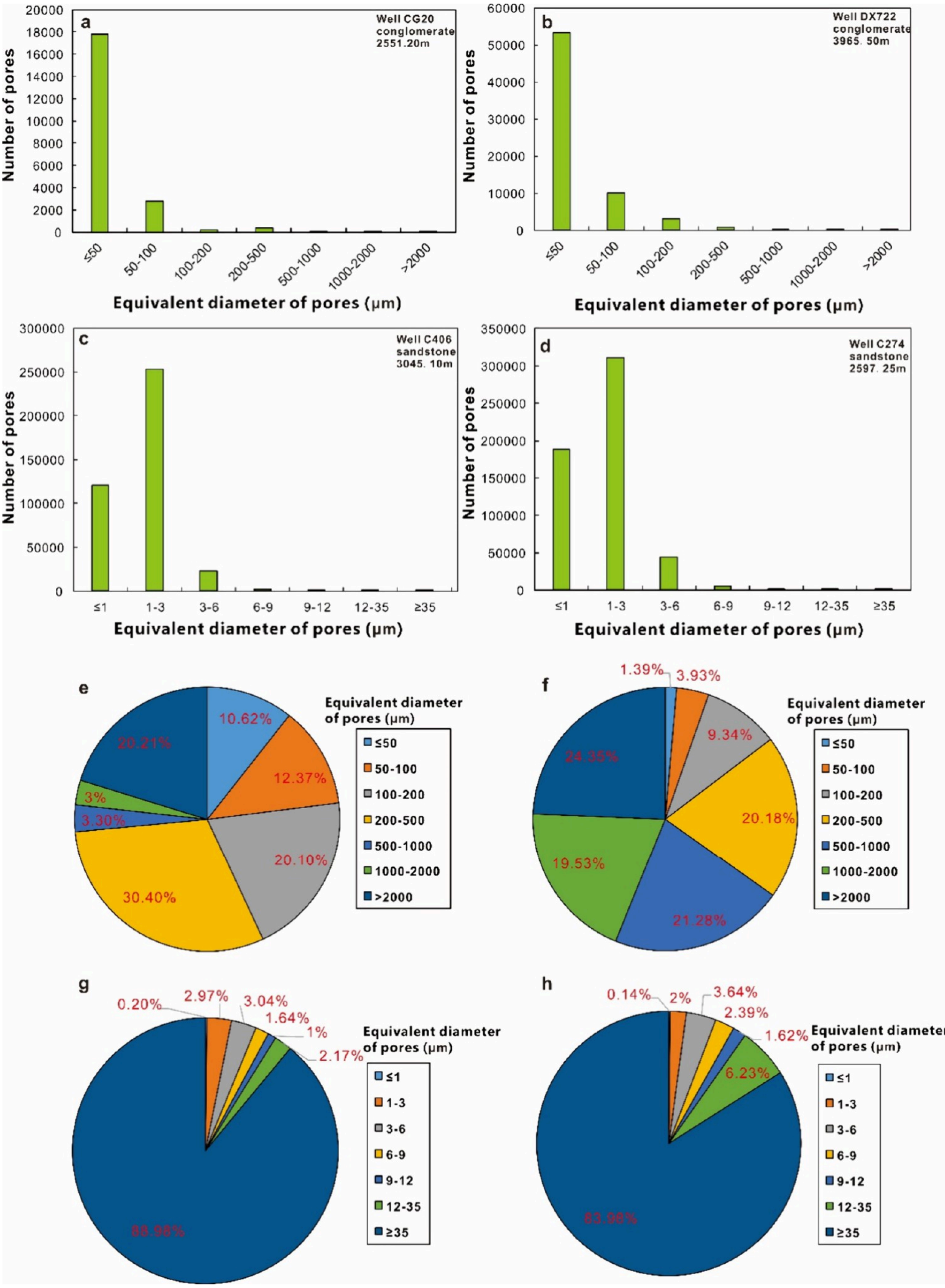

Figure 5. Histogram of the number of pores of various diameters in the (a) conglomerate reservoir in Well CG20; (b) conglomerate reservoir in Well DX722; (c) sandstone reservoir in Well C406; and (d) sandstone reservoir in Well C274 and pore volume proportion in the (e) conglomerate reservoir in Well CG20; (f) conglomerate reservoir in Well DX722; (g) sandstone reservoir in Well C406; and (h) sandstone reservoir in Well C274.

although the number of pores has grown (accounting for 1.49% of the total volume) and cements are sparsely dispersed (accounting for 0.05% of the total volume) (Figure 4(d) and Table 1). The isolated pores in the sandstone reservoirs in the central depression zone of the Chexi Subsag have drastically diminished (Figure 4(e)). In addition, the cement content

https://doi.org/10.1021/acsomega.4c02106
ACS Omega 2024, 9, 22952−22969

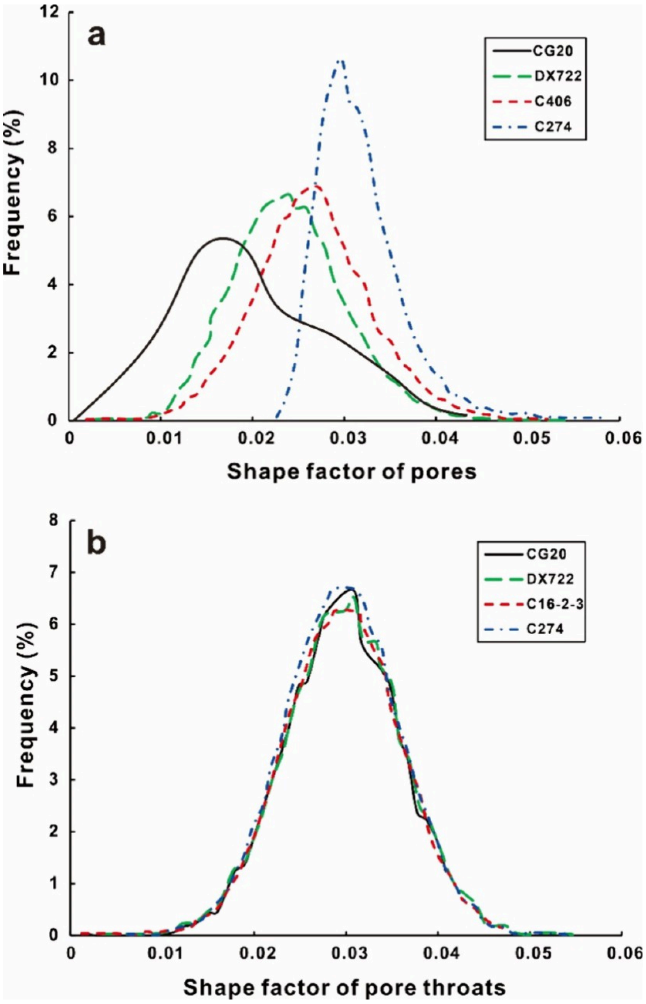

Figure 6. Distribution of the shape factor of pores (a) and pore throats (b).

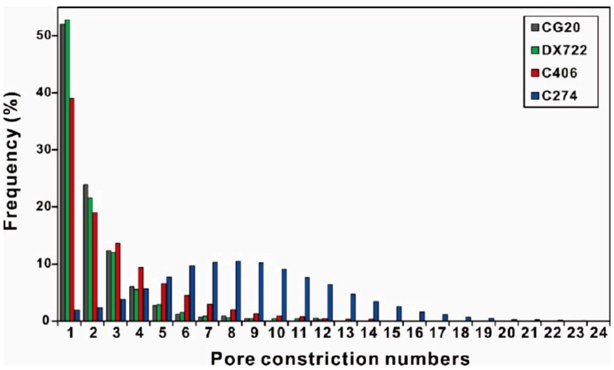

Figure 7. Distribution of pore coordination numbers in the conglomerate and sandstone reservoirs in the Chezhen Sag.

(accounting for 17.53% of the total volume) has increased significantly (Figure 4(f) and Table 1). The sandstone reservoirs in the gentle slope zone have the lowest number of isolated pores (Figure 4(g)), a moderate cement content (accounting for 4.87% of the total volume), and the highest proportion of pores (accounting for 7.15% of the total volume) (Figure 4(h) and Table 1). Overall, a sandstone reservoir has a lower number of isolated pores and a larger fraction of pore volume than a conglomerate reservoir. In the north−south direction, the reservoir porosity increases when moving from the steep slope zone to the gentle slope zone because of the increase in the proportion of connected pores (Figure 4).

4.2. Pore Size and Pore Size Distribution. Sieving statistical analysis was performed on the number of pores for various pore dimensions (Table 1). The results indicated that conglomerate samples have a maximum diameter of 2,000 μm and the highest number of pores at diameters below 50 μm (Figure 5(a) and (b)). The number of pores in each diameter range in the conglomerate in Well DX722 is higher than that in Well CG20 (Figure 5(a) and (b)), indicating that the conglomerate reservoir in the steep slope zone of the Dawangbei Subsag is more porous than that in the western Chexi Subsag. Pore diameters in the sandstone samples are typically less than 35 μm with most of the pores having a diameter between 1 and 3 μm (Figure 5(c) and (d)). The sandstone reservoir in the gentle slope zone has better porosity than that in the depression zone, the number of pores of each diameter grade in Well C274 being higher than that in Well C406 (Figure 5(c) and d)). The conglomerate reservoir in Well CG20 has the highest proportion of pores with diameters between 200 and 500 μm (accounting for 30.45%) (Figure 5(e)), whereas the conglomerate reservoir in Well DX722 has the highest proportion of pores with diameters exceeding 2000 μm (Figure 5(f)). The pore volumes of the sandstone reservoirs in Wells C406 and C274 are both dominated by pores larger than 35 μm in diameter (accounting for 85.99% and 83.98%, respectively) as can be seen in Figure 5(g) and (h). In general, in both sandstone and conglomerate reservoirs, the number of small pores dominates the total number of pores, whereas large pores make up most of the total pore volume. Additionally, the number of pores in sandstone reservoirs is significantly higher than that in conglomerate reservoirs. The number of pores in conglomerate reservoirs in the steep slope zone increases in the west to east direction, while the number of pores when moving from the steep slope zone to the gentle slope zone grows from south to north. The quantitative statistical findings are consistent with 3D characterization results.

4.3. Geometry of the Pores and Pore Throats. The pore and throat shapes are frequently simplified to represent cross-sectional shapes considering the complicated shapes of the actual pores and throats. The application of the shape factor (G) enables the quantitative analysis of pore and pore throat shapes.[44] The G value, which characterizes the geometry of the pore and pore throat cross sections, is calculated as follows:

$$G = \frac{A}{P^2} \tag{1}$$

where A is the cross-sectional area of the pores/throats in μm^2 and P is the perimeter of the pores/throats in μm. The geometry of the pores/throats will become more consistent with the increase in the shape factor.[45−49] The G value of a triangle depends on the size of its interior angle, and its value falls in the range from 0 to 0.0481. The G value of a rectangle is between 0.0481 and 0.071, and that of a circle is 0.0796.[44]

In the study, the pore G values (PGV) of the conglomerate in Well CG20 was between 0.0012 and 0.0424 with an average of 0.0216. The PGV of the conglomerate in Well DX722 was between 0.0030 and 0.0544 with an average of 0.0284. The PGV of sandstone in Well C406 was in the range from 0.0019 to 0.0566 with an average of 0.0282. The PGV of sandstone in

https://doi.org/10.1021/acsomega.4c02106
ACS Omega 2024, 9, 22952−22969

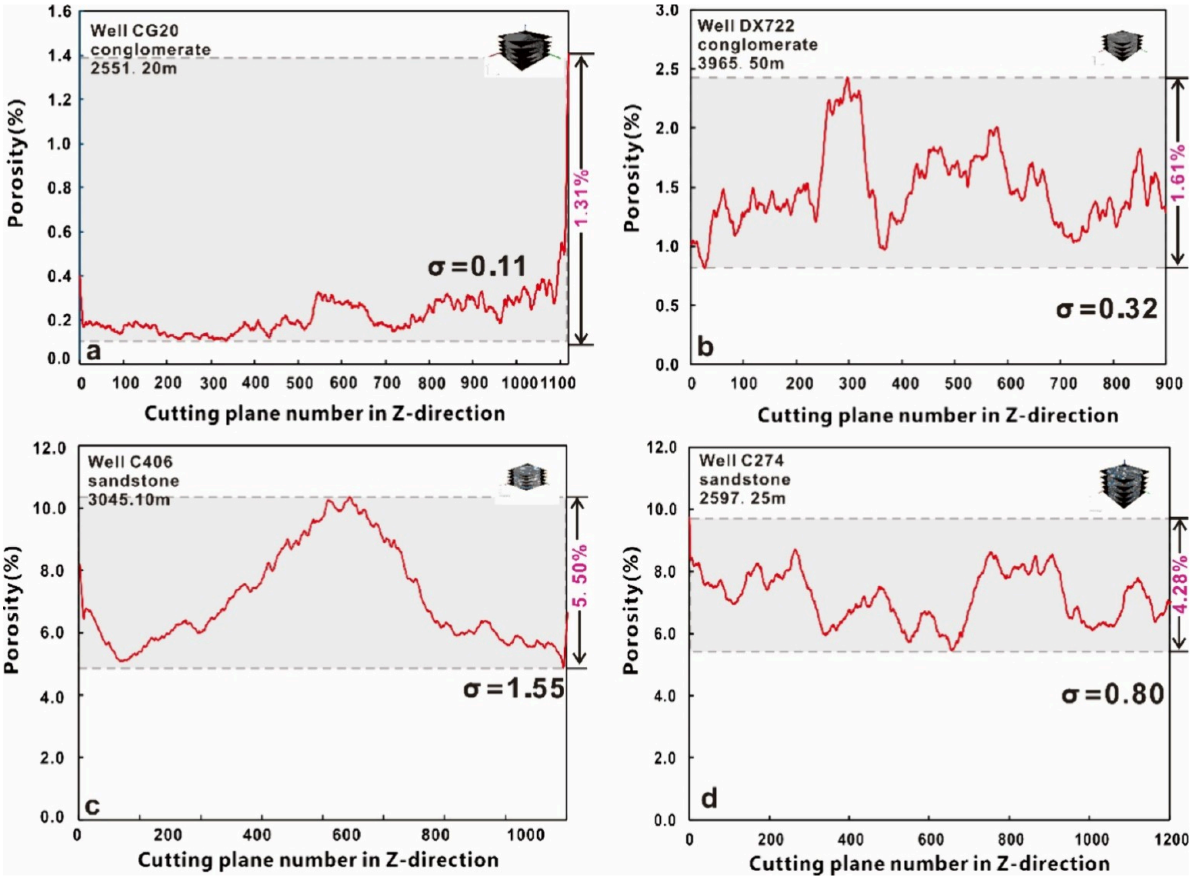

Figure 8. Layer-by-layer porosity distribution of the conglomerate reservoirs of Well CG20 (a) and Well DX722 (b) and sandstone reservoirs of Well C406 (c) and Well C274 (d) in the Chezhen Sag along the *Z*-axis. σ refers to the standard deviation.

Well C274 was between 0.0221 and 0.0577 with an average of 0.0387 (Figure 6(a)). These pore shape factor data reveal that the pores of the sandstone and conglomerate reservoirs in the Chezhen Sag are primarily triangular in shape and that the pores of the sandstone reservoirs are more regular than the pores of the conglomerate reservoirs. The sandstone reservoir of Well C274 in the gentle slope zone has the most concentrated range of PGV and the highest average value (Figure 6(a)), indicating the lowest change in the pore shape. By contrast, the conglomerate reservoir in Well CG20 in the steep slope zone has the widest PGV range and the smallest average of PGV (Figure 6(a)), indicating complex pore geometries and high heterogeneity. However, only little distinction exists between the pore throat G values (PTGV) of sandstone reservoirs and those of conglomerate reservoirs (Figure 6(b)). The PTGV are regularly distributed, and more than 95% of the pore throat shape factors are less than 0.0481, showing that triangles dominate the geometry of pore throats in the sandstone and conglomerate reservoirs.

4.4. Pore Connectivity. The coordination number can characterize the connectivity of pores to some degree.[50−52] The pore coordination number (PCN) refers to the number of pore throats connected to a single pore.[53,54] The PCN of dead pores is 0, and the PCN of pores with a dead end is 1. Therefore, the PCN of connected pores should be higher than 1, and the larger the PCN is, the better will be the connectivity of the pores.

In this study, the PCN of the conglomerate reservoir in Well CG20 was found to vary between 1 and 10, the pores with dead ends accounted for the largest proportion (52.01%), and the connected pores accounted for 47.99% (Figure 7). The PCN of the conglomerate reservoir in Well DX722 was in the range from 1 to 12, the proportion of pores with dead ends was 52.84%, and the proportion of connected pores was 47.16% (Figure 7). The PCN of the sandstone reservoir in Well C406 was in the range between 1 and 18, and the pores with dead ends continued to have the highest proportion, accounting for 37.44% (Figure 7). However, the proportion of connected pores grew dramatically to reach 62.56%. The PCN of the sandstone reservoir in Well C274 was in the range from 1 to 24 (Figure 7). Its pores with dead ends accounted only for 1.94%, and the connected pores accounted for 98.06%. Among them, the pores with a PCN of 8 accounted for the largest proportion with a value of 10.5%. From the perspective of PCN distribution, the connectivity of pores in sandstone reservoirs is considerably superior to that of conglomerate reservoirs. The reservoirs in the gentle slope zone have the best pore connectivity, followed by the reservoirs in the central depression zone and the poorest in the steep slope zone.

4.5. Heterogeneity of Reservoir Porosity. The layer-by-layer porosity (LBLP) distribution in the direction of the *Z*-axis varies considerably among the reservoirs that have diverse lithologies and secondary structural zones. The LBLP of the conglomerate from Well CG20 is in the range from 0.14% to 1.4%, and most of the porosity values fluctuate between 0.2% and 0.4% (Figure 8(a)). The standard deviation (σ) of the porosity of 1120 tomograms is 0.11, indicating that the conglomerate reservoir in the steep slope zone of the Chexi

https://doi.org/10.1021/acsomega.4c02106
ACS Omega 2024, 9, 22952−22969

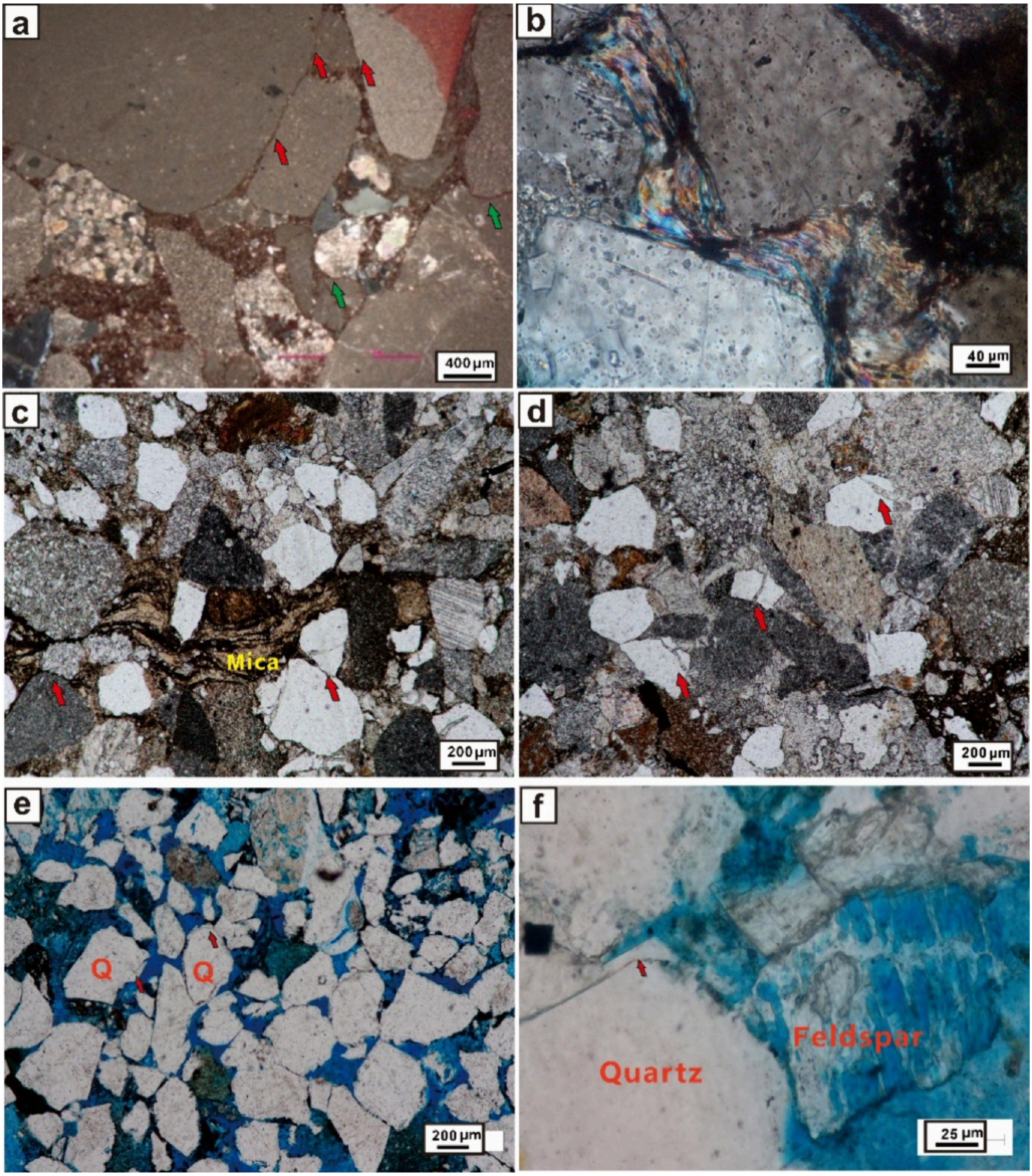

Figure 9. Optical photomicrographs showing the diagenesis in different secondary structural zones. (a) The diameter of the debris particles is relatively large, with the particle line contact (red arrow), and the concave convex contact (green arrow) can be seen, plane-polarized light (PPL), Well CG25, 4343.53 m. (b) Mica undergoes severe deformation under mechanical compaction, cross-polarized light (CPL), Well C57, 4217.78 m. (c) High content of rock debris, particles not in contact or in line contact (red arrow), mica compacted, fractured, and deformed, PPL, Well C660, 4141.20 m. (d) Rigid particles form fractures under mechanical compaction and are later filled with cements, PPL, Well C660, 4141.20 m. (e) Mainly intergranular pores with good pore connectivity, developed quartz overgrowth (red arrow), PPL, Well C276, 2449.5 m. (f) Quartz overgrowth (red arrow) adjacent to feldspar dissolution zone, PPL, Well C142−41, 2915.10 m.

Subsag is tight and homogeneous. The LBLP of the conglomerate from Well DX722 is in the range from 0.8% to 2.5% with an increased volatility and a standard deviation of 0.32 (Figure 8(b)). The porosity of the conglomerate reservoir has marginally improved in the direction from west to east; the heterogeneity of the reservoir also has improved and the

https://doi.org/10.1021/acsomega.4c02106
ACS Omega 2024, 9, 22952−22969

Table 2. Results of Point Counting for Detrital Composition and Derived Parameter Data of Conglomerate and Sandstone Reservoirs in the Chezhen Sag[a]

Well	Depth (m)	Q (%)	F (%)	RF (%)	VRF (%)	MRF (%)	SRF (%)	So	I.P (%)	A.P (%)	P.P (%)	S.P (%)	P.Ce (%)	ACoR (%)	ACeR (%)	ADR (%)
CG20	2551.21−2551.82	40.00	28.00	32.00	8.00	10.00	14.00	1.51	36.08	4.20	1.00	3.20	0.20	96.67	16.67	76.19
CG20	2551.21−2551.82	25.00	25.00	50.00	13.00	15.00	22.00	1.62	35.05	5.10	1.50	3.60	0.40	94.58	21.05	70.59
CG20	2551.21−2551.82	15.00	10.00	75.00	5.00	15.00	55.00	1.71	34.30	0.10	0.00	0.10	0.00	100.00	0.00	100.00
CG20	2551.21−2551.82	40.00	28.00	32.00	3.00	13.00	16.00	1.56	35.59	1.20	0.12	1.08	0.05	99.52	29.41	90.00
CG20	2551.21−2551.82	35.00	18.00	47.00	8.00	15.00	24.00	1.76	33.92	2.10	0.21	1.89	0.06	99.20	22.22	90.00
CG20	2551.21−2551.82	32.00	23.00	45.00	10.00	16.00	19.00	1.59	35.31	2.20	0.40	1.80	0.15	98.44	27.27	81.82
CG20	2551.21−2551.82	35.00	30.00	35.00	6.00	13.00	16.00	1.56	35.59	2.50	0.40	2.10	0.10	98.60	20.00	84.00
DX722	3965.32−3965.75	30.00	22.00	48.00	2.00	38.00	8.00	1.45	36.70	1.96	1.70	0.26	1.20	92.10	41.38	13.27
DX722	3965.32−3965.75	26.00	8.00	66.00	5.00	50.00	11.00	1.52	35.98	2.06	1.80	0.26	0.90	92.49	33.33	12.62
DX722	3965.32−3965.75	30.00	15.00	55.00	4.00	20.00	31.00	1.46	36.59	5.40	4.45	0.95	1.10	84.83	19.82	17.59
DX722	3965.32−3965.75	54.00	31.00	15.00	4.00	10.00	1.00	1.45	36.70	6.50	5.60	0.90	3.50	75.21	38.46	13.85
DX722	3965.32−3965.75	53.00	32.00	15.00	5.00	8.00	2.00	1.39	37.38	7.80	7.10	0.70	4.00	70.31	36.04	8.97
DX722	3965.32−3965.75	48.00	41.00	11.00	0.00	10.00	1.00	1.44	36.81	3.22	3.10	0.12	2.50	84.79	44.64	3.73
DX722	3965.32−3965.75	36.00	37.00	27.00	3.00	5.00	19.00	1.56	35.59	2.56	2.45	0.11	3.14	84.29	56.17	4.30
DX722	3965.32−3965.75	33.00	37.00	30.00	4.00	6.00	20.00	1.45	36.70	6.52	5.98	0.54	2.56	76.73	29.98	8.28
DX722	3965.32−3965.75	30.00	38.00	32.00	5.00	6.00	21.00	1.46	36.59	2.10	2.01	0.09	1.58	90.19	44.01	4.29
C406	3044.82−3045.34	45.00	26.00	29.00	5.00	14.00	10.00	1.36	37.75	3.64	3.11	0.53	1.80	86.99	36.66	14.56
C406	3044.82−3045.34	48.00	25.00	27.00	5.00	12.00	10.00	1.38	37.50	8.40	6.45	1.95	2.90	75.07	31.02	23.21
C406	3044.82−3045.34	52.00	22.00	26.00	6.00	11.00	9.00	1.34	38.00	10.20	8.21	1.99	3.20	69.97	28.05	19.51
C406	3044.82−3045.34	55.00	18.00	27.00	7.00	15.00	5.00	1.33	38.13	9.85	7.21	2.64	2.50	74.53	25.75	26.80
C406	3044.82−3045.34	59.00	17.00	24.00	4.00	12.00	8.00	1.36	37.75	8.65	6.24	2.41	3.60	73.93	36.59	27.86
C406	3044.82−3045.34	65.00	8.00	27.00	2.00	15.00	10.00	1.35	37.87	5.69	4.22	1.47	2.10	83.31	33.23	25.83
C406	3044.82−3045.34	68.00	5.00	27.00	3.00	16.00	8.00	1.36	37.75	7.65	5.46	2.19	4.00	74.94	42.28	28.63
C274	2597.14−2597.64	67.00	12.00	21.00	3.00	15.00	3.00	1.26	39.08	14.20	8.20	6.00	2.12	73.60	20.54	42.25
C274	2597.14−2597.64	60.00	10.00	30.00	3.00	21.00	6.00	1.23	39.53	12.50	7.10	5.40	1.56	78.09	18.01	43.20
C274	2597.14−2597.64	63.00	15.00	22.00	3.00	17.00	2.00	1.25	39.23	14.50	8.00	6.50	2.58	73.03	24.39	44.83
C274	2597.14−2597.64	61.00	11.00	28.00	8.00	15.00	5.00	1.24	39.38	15.60	10.01	5.59	1.05	71.91	9.49	35.83
C274	2597.14−2597.64	66.00	11.00	23.00	4.00	16.00	3.00	1.29	38.66	15.20	7.99	7.21	0.98	76.80	10.93	47.43
C274	2597.14−2597.64	64.00	11.00	25.00	4.00	19.00	2.00	1.25	39.23	14.20	7.66	6.54	0.85	78.31	9.99	46.06
C274	2597.14−2597.64	67.00	12.00	21.00	3.00	14.00	4.00	1.30	38.53	15.20	7.56	7.64	2.54	73.78	25.15	50.26
C274	2597.14−2597.64	65.00	10.00	25.00	4.00	18.00	3.00	1.24	39.38	16.40	9.45	6.95	3.56	66.96	27.36	42.38
C274	2597.14−2597.64	61.00	11.00	28.00	8.00	15.00	5.00	1.26	39.08	12.10	7.21	4.89	1.78	77.00	19.80	40.41
C274	2597.14−2597.64	60.00	10.00	30.00	3.00	22.00	5.00	1.25	39.23	10.20	6.05	4.15	2.10	79.23	25.77	40.69
C274	2597.14−2597.64	62.00	16.00	22.00	3.00	15.00	4.00	1.26	39.08	9.50	5.31	4.19	0.89	84.14	14.35	44.11
C274	2597.14−2597.64	66.00	12.00	22.00	4.00	15.00	3.00	1.27	38.94	8.25	5.54	2.71	1.02	83.15	15.55	32.85

[a]Q = quartz; F = feldspar; RF = rock fragments; VRF = volcanic rock fragments; MRF = metamorphic rock fragments; SRF = sedimentary rock fragments; So = sorting coefficient; I.P = initial porosity; A.P = apparent porosity; P.P = primary porosity; S.P = secondary porosity; P.Ce = porosity occupied by cements; ACoR = apparent compaction rate; ACeR = apparent cementation rate; ADR = apparent dissolution rate. Note: I.P = 20.91 + 22.90/So; A.P = P.P + S.P; P.P, S.P, and P.Ce were determined by point counting.

https://doi.org/10.1021/acsomega.4c02106
ACS Omega 2024, 9, 22952−22969

conglomerate reservoir exhibits tight features. The LBLP of sandstone from Well C406 is in the range from 5% to 11%, with a high overall variability along the Z-axis (Figure 8(c)). The standard deviation of the porosity of 776 tomograms is 1.55, which is much higher than that of conglomerate reservoirs. The porosity of the sandstone in Well C274 falls in the range from 5% to 10% in the direction of the Z-axis, and most of the porosity values fluctuate between 6% and 8% with a standard deviation of 0.80 (Figure 8(d)). In this study, the sandstone reservoirs were found to be more porous than the conglomerate reservoirs, but the sandstone reservoirs were also found to have higher heterogeneity than the conglomerate reservoirs.

4.6. Diagenesis in Different Secondary Structural Zones. Based on thin section observation, it can be seen that the debris particles in the steep slope reservoir are mainly in linear contact (Figure 9a). In the later stage of mechanical compaction, chemical compaction occurs, resulting in a concave convex contact between particles (Figure 9a). And when the mica content is high, compaction deformation of mica is common (Figure 9b). The rigid particles in the reservoir within the depression zone have increased, but compaction still dominates. The clastic particles are mainly in line contact, and it can be seen that mica has undergone compaction deformation and even been fractured (Figure 9c). Meanwhile, the rigid particles in the area with intense compaction fractured and are later filled with cements (Figure 9d). The compaction is weak in the gentle slope zone, and primary pores dominate (Figure 9e). Secondary pores are developed in areas with strong dissolution, and quartz-overgrowth are often developed adjacent to the dissolution area (Figure 9f).

5. DISCUSSION

5.1. Effect of Depositional Environment and Mineral Composition on the Heterogeneity of Initial Reservoir Porosity. In this study, the reservoir samples from four wells were selected for thin section observation, and the results are shown in Table 2. The type of the parent rock, mineral composition of the reservoir rocks, and transport distance of clastic rock reservoirs control the maturity and sorting behavior of the reservoirs, which in turn affects their initial porosity and pore evolution processes.[4,55,56]

As the transportation distance increases, the content of unstable components gradually decreases, and sorting is improved.[23,57,58] Delta is primarily developed in the gentle slope zone of the Chezhen Sag, whereas alluvial fan and fan delta are developed in its steep slope and depression zones.[41] Alluvial fans and fan deltas are adjacent to provenance and are characterized by large grain size and low compositional maturity. The reservoirs in CG20 and DX722 wells are typical fan delta deposits with low compositional maturity (Figure 10(a)). Based on the results of the wet packing experiment,[55,56] the initial porosity of the selected four samples can be calculated. The initial porosity of conglomerate reservoirs is low (average = 35.12%) because of poor sorting. Some samples from Well DX722 include much more metamorphic rock fragments than the samples from Well CG20 do, suggesting that the types of parent rock in these samples are more complicated (Figure 10(b)). Because of the resistance displayed by metamorphic rock fragments to compaction, the initial porosity of the conglomerate reservoir in Well DX722 is higher than that in Well CG20 (average = 36.56). The

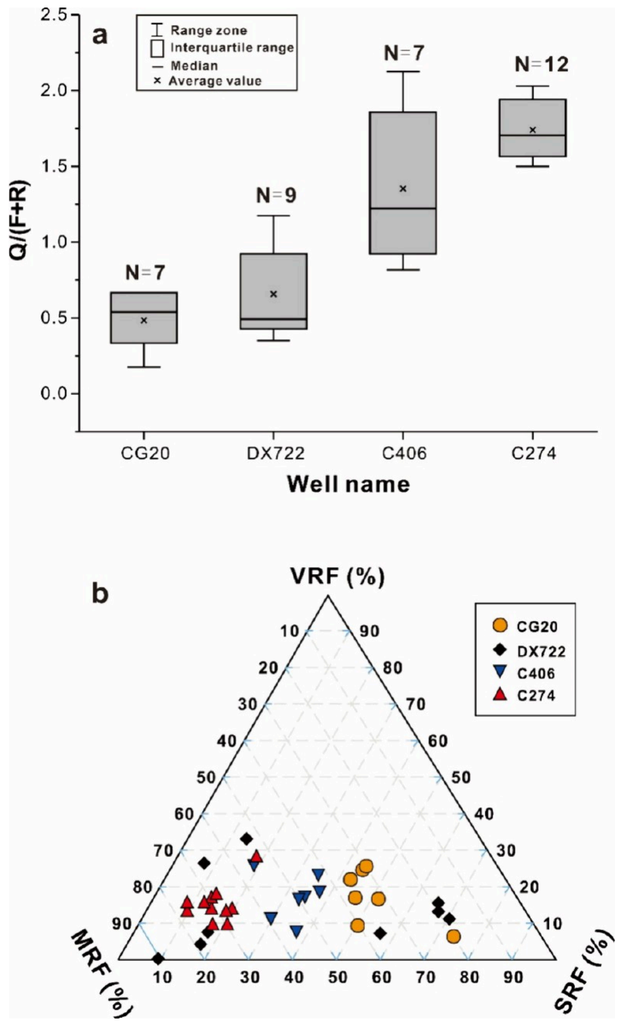

Figure 10. (a) Box diagram of Q/(F + R) indicating the compositional maturity of the conglomerate reservoirs in Well CG20 and Well DX722 and sandstone reservoirs in Well C406 and Well C274. Q = quartz; F = feldspar; R = rock fragments. (b) Rock fragment ternary plots of the rock fragments in the conglomerate and sandstone reservoirs in the Chezhen Sag. (VRF = volcanic rock fragments; MRF = metamorphic rock fragments; and SRF = sedimentary rock fragments).

compositional maturity of the reservoir of Well C406 in the depression zone grows with increasing transportation distance with the initial porosity also increasing (average = 37.82). The sandstone reservoir of Well C274 in the gentle slope zone has the highest compositional maturity with a large content of rigid grains (Figure 10(b)). Its initial porosity is therefore the best (average = 39.11%).

5.2. Effect of Diagenetic Intensity on the Differential Evolution of Reservoir Porosity. The initial porosity of a reservoir is determined by its depositional environment and provenance type, whereas its evolution is determined by diagenetic type and intensity.[58−60] Compaction and cementation can often cause a loss in reservoir porosity, while dissolution can have complex consequences on reservoir physical parameters under various diagenetic conditions.[61−63] The apparent compaction rate (ACoR), apparent cementation rate (ACeR), and apparent dissolution rate (ADR) were used to describe the effects of various diagenetic conditions on reservoir quality.[64] The following formula can be used to

https://doi.org/10.1021/acsomega.4c02106
ACS Omega 2024, 9, 22952−22969

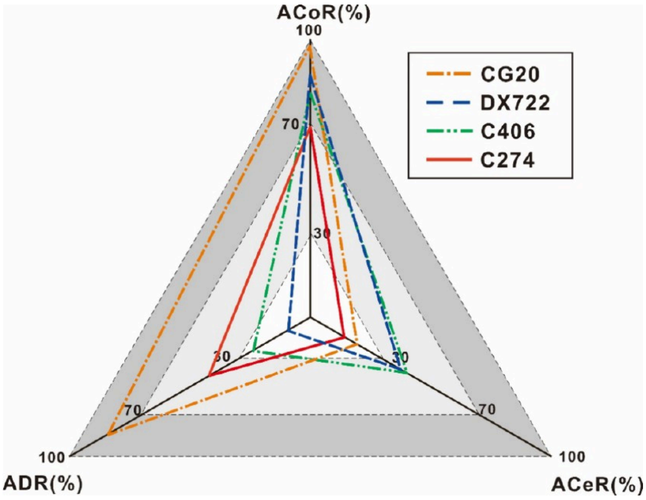

Figure 11. Radar map of the apparent compaction rate, apparent cementation rate, and apparent dissolution rate characterizing the intensity of compaction and cementation and the degree of reservoir stimulation caused by dissolution.

calculate the ACoR, which is used to quantitatively describe compaction intensity:

$$\mathrm{ACoR} = \frac{P_I - P_P - P_{Ce}}{P_I} \times 100\% \tag{2}$$

where P_I is the initial porosity, P_P is the primary porosity after compaction, and P_{Ce} is the porosity occupied by the cements. In this study, severe compaction was indicated by an ACoR exceeding 70%, moderate compaction by an ACoR between 30% and 70%, and weak compaction by an ACoR below 30%.

The ACeR measures how much cementation has affected the initial porosity of the reservoir. It can be calculated using the following formula:

$$\mathrm{ACeR} = \frac{P_{Ce}}{P_P + P_{Ce}} \times 100\% \tag{3}$$

In this study, cementation was considered severe when the ACeR was greater than 70%, moderate when the ACeR was between 30% and 70%, and weak when the ACeR was below 30%.

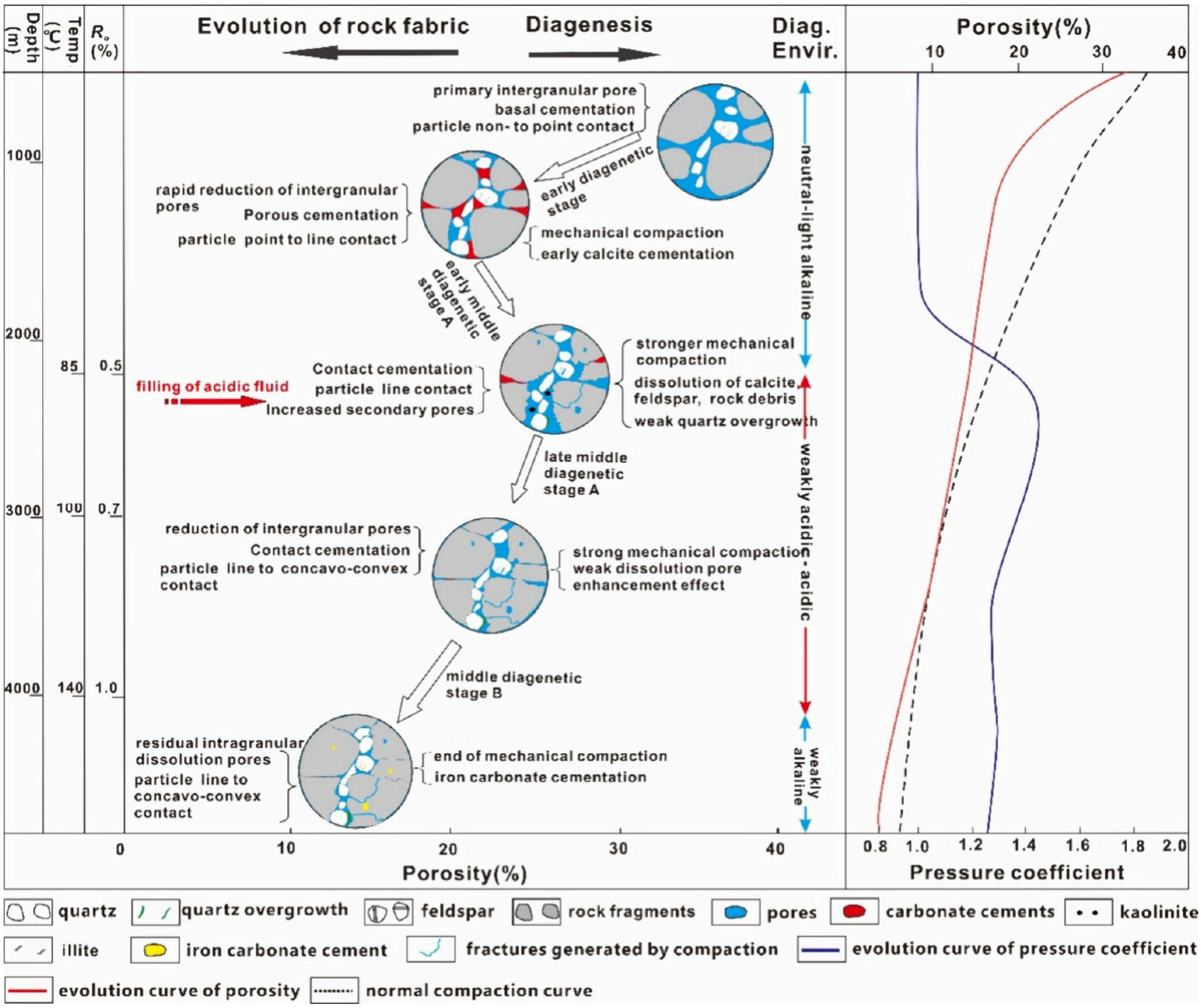

Figure 12. History of the reservoir porosity evolution of Well CG 20 in the steep slope zone of the Chezhen Sag. Temp. = Temperature; Diag. Envir. = Diagenetic environment.

https://doi.org/10.1021/acsomega.4c02106
ACS Omega 2024, 9, 22952−22969

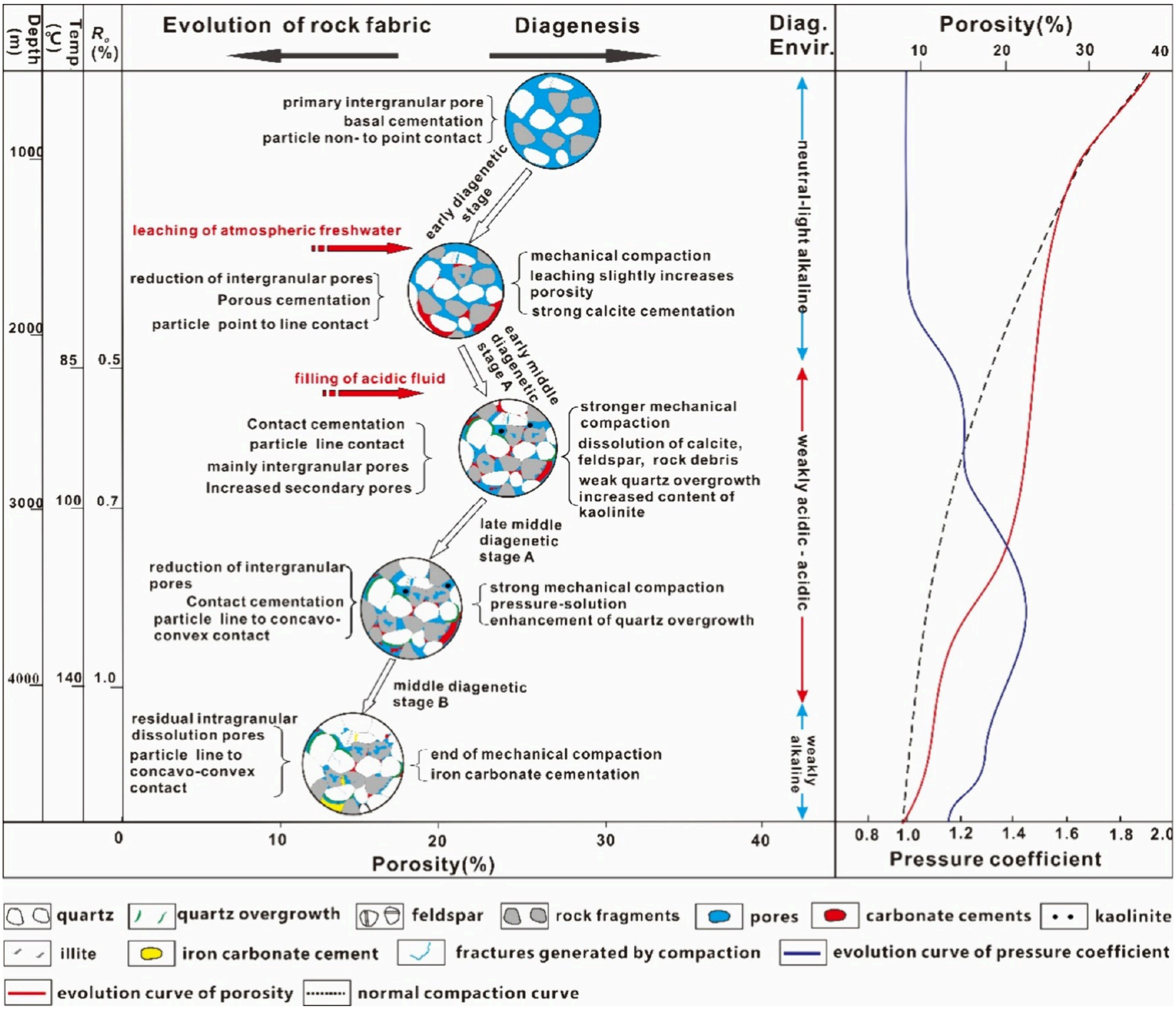

Figure 13. History of the reservoir porosity evolution of Well DX722 in the steep slope zone of the Chezhen Sag. Temp. = Temperature; Diag. Envir. = Diagenetic environment.

The ADR is used to quantify the proportion of secondary porosity in the total porosity indicating the degree of transformation of reservoir pore space due to dissolution. It can be calculated using the following formula:

$$\mathrm{ADR} = \frac{P_S}{P_P + P_S} \times 100\% \tag{4}$$

where P_S is the secondary porosity.

To quantify the diagenetic intensity of different reservoirs, three-end-member radar maps of the reservoir ACoR, ACeR, and ADR were prepared (Figure 11). The conglomerate reservoir in Well CG20 in the steep slope zone is characterized with a high proportion of secondary porosity (an average ADR of 84.66%), weak cementation (an average ACeR of 19.52%), and severe compaction (an average ACoR of 98.15%). The conglomerate reservoir in Well DX722 in the steep slope zone displays strong compaction (an average ACoR of 83.44%), moderate cementation (an average ACeR of 38.20%), and a low proportion of secondary porosity (an average ADR of 9.56%). The sandstone reservoir in Well C406 in the steep slope zone displays strong compaction (an average ACoR of 76.96%), moderate cementation (an average ACeR of 33.37%), and a higher proportion of secondary porosity (an average ADR of 23.77%). The sandstone reservoir in Well C274 in the gentle slope zone exhibits weaker compaction (an average ACoR of 76.33%) than other reservoir samples, weak cementation (an average ACeR of 18.44%), and the highest proportion of secondary porosity (an average ADR of 42.52%).

This study quantified the diagenetic-porosity differential evolution history of the reservoirs in the Chezhen Sag using the calculation method proposed by Li et al., (2017). The conglomerate reservoir of Well CG20 in the steep slope zone contains a large amount of matrix with weak resistance to compaction. Its porosity decreased to 19.15% in the early diagenetic stage owing to mechanical compaction. Cementation has little impact on the loss of reservoir porosity (porosity after early cementation is 17.56%) because of low pore connectivity and restricted material transmission. The porosity continued to decrease with compaction, leading to the poor reservoir quality and a porosity of 4.54% (Figure 12).

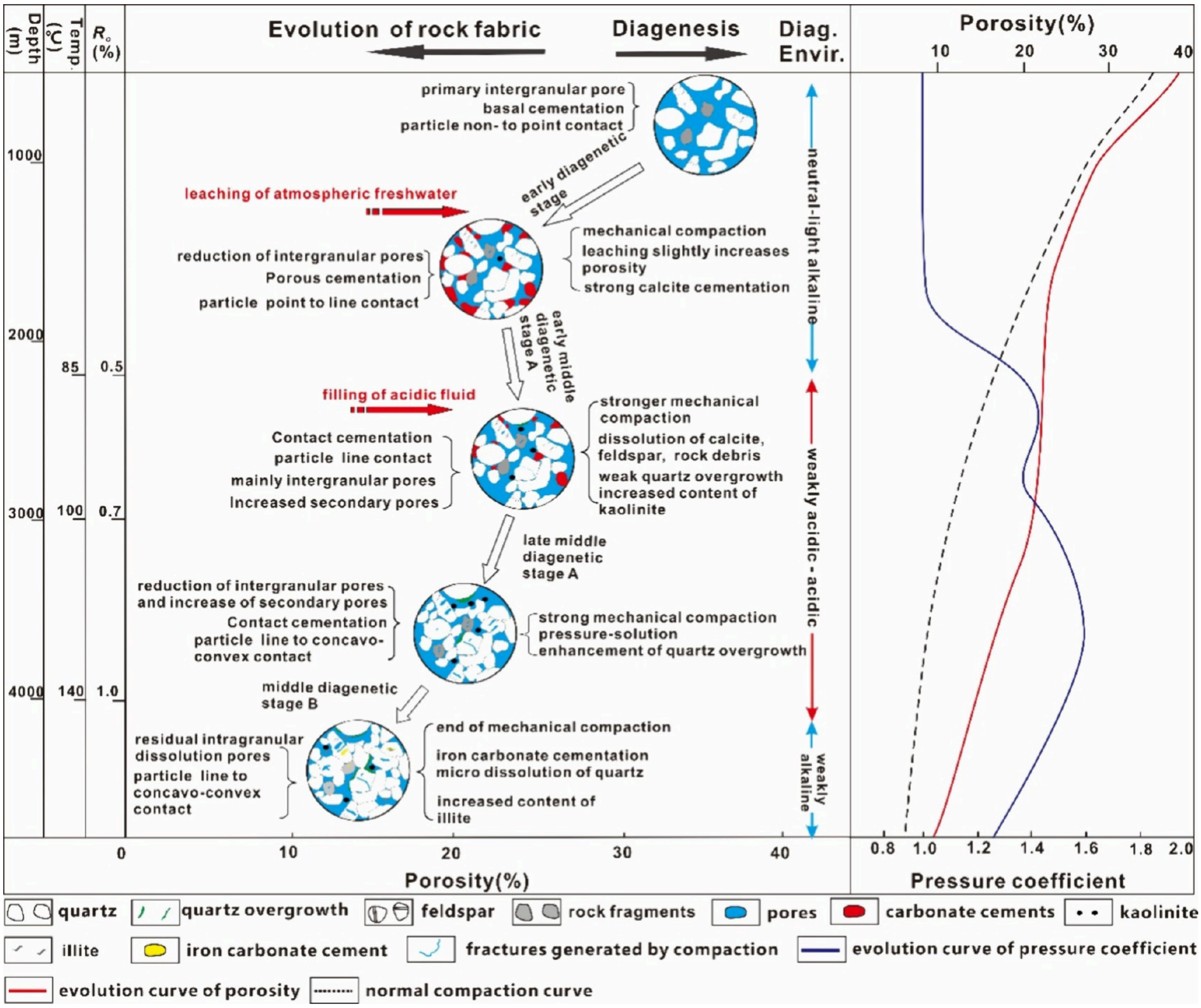

Figure 14. History of the reservoir porosity evolution of Well C406 in the depression zone of the Chezhen Sag. Temp.=Temperature; Diag. Envir.=Diagenetic environment.

The relatively higher compositional maturity strengthened the resistance of the sandstone reservoir in Well DX722 owing to compaction, allowing for the preservation of 25.32% of the porosity even after early compaction. Cementation and dissolution of the reservoir are weak as a result of poor pore connectivity, and the final porosity is 8.67% (Figure 13).

Despite having a high compositional maturity, the sandstone reservoir of Well C406 in the depression zone loses 10.37% of its porosity in the early diagenetic stage. The reservoir porosity has become worse because of cementation. Because of the confined diagenetic environment, dissolution has only little impact on reservoir reformation. Finally, the porosity of the reservoir in the depression was preserved at 10.14% (Figure 14).

As a result of shallow burial depth, the highest compositional maturity, and well sorting, the porosity of the sandstone reservoir in the gentle slope zone retains 30.45% of its initial porosity after early compaction. The superior pore connectivity of the reservoir facilitates fresh water and acidic fluids to migrate into it, allowing the early dissolution of unstable components, such as cements, feldspars, and rock fragments. Because dissolution products are carried away from the reservoir in an open diagenetic environment,[65] the dissolution effectively improves the physical properties of the reservoir. The reservoir in the gentle slope zone has a porosity of 12.45% owing to the combined effect of these favorable conditions (Figure 15). Above all, dissolution does not significantly improve reservoir porosity in most cases, but it rather decreases the rate at which compaction and cementation reduce reservoir porosity. Dissolution can enhance reservoir porosity in an open diagenetic environment with good pore connectivity and widely distributed primary and secondary pores.

5.3. Quantitative Assessment of Reservoir Quality Based on Pore Types. Besides mineral intercrystalline pores, the pores of clastic rock reservoirs can be divided into primary pores and secondary pores.[66,67] Primary pores are the intergranular pores that remain in the reservoir after compaction and cementation. Secondary pores are intragranular and intergranular pores that form as a result of dissolution. In this study, pores with residual mineral can be definitively defined as secondary pores. Intergranular pores with regular shapes are usually defined as primary pores, while pores with irregular shapes accompanied by clay mineral

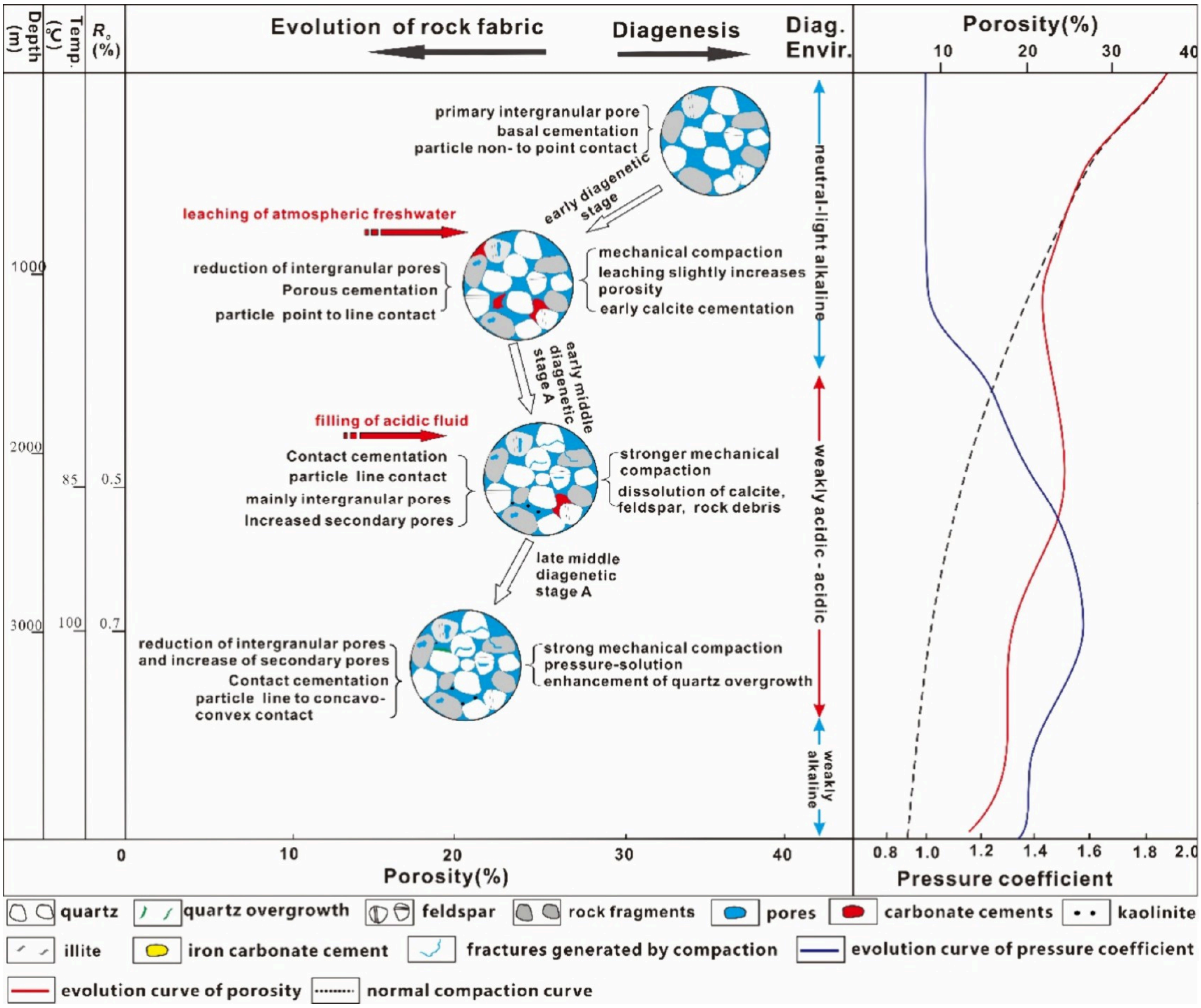

Figure 15. History of the reservoir porosity evolution in the gentle slope zone of the Chezhen Sag. Temp. = Temperature; Diag. Envir. = Diagenetic environment.

precipitation and quartz-overgrowth are defined as mixed pores of primary and secondary pores. The total volume of primary and secondary pores can indicate reservoir quality, whereas the relative volume of primary and secondary pores can reflect to some extent the evolution mechanism of reservoir porosity. This study proposed a method for the classification of reservoirs based on their pore types.

First, the primary and secondary porosities of the reservoir were determined using thin section observation and point counting. Following that, a bubble map depicting the distribution of reservoir porosity was created using the parameters primary porosity, secondary porosity, and total porosity (Figure 16). The abscissa and ordinate were primary porosity and secondary porosity, respectively, and the bubble size represented the total porosity. In this study, a reservoir with a total porosity below 5% was considered a tight reservoir, a reservoir with a total porosity between 5% and 10% a low porosity reservoir, and a reservoir with a total porosity between 10% and 15% a medium porosity reservoir. A reservoir was considered to possess high porosity if its total porosity was higher than 15%. By marking the boundary lines in the bubble chart with total porosity values of 5%, 10% and 15%, the distribution zones of various reservoir levels can be separated. By entering the primary and secondary porosity data into the bubble chart, the quality of the reservoir can be rapidly evaluated, and the influence of dissolution on the quality of the reservoir can be determined.

The conglomerate reservoir in Well CG20 is a typical tight reservoir with many secondary pores and almost no primary pores (Figure 16). The conglomerate reservoir in Well DX722 is a tight reservoir with low porosity. The pores of the conglomerate reservoirs in Well DX722, which are also tight reservoirs, are dominated by primary pores (Figure 16), indicating that dissolution is weak in them and that compaction and cementation dominate reservoir porosity evolution. The quality of the sandstone reservoir in Well C406 is slightly better than that in Well DX722, which is also dominated by primary pores (Figure 16). The sandstone reservoirs in Well C274 are mainly medium to high porosity reservoirs (Figure 16). Despite being dominated by primary pores, their secondary porosity is also high, suggesting weak compaction and cementation and strong dissolution.

A special type of reservoir was discovered in this study: the tight conglomerate reservoir in Well CG20. As previously

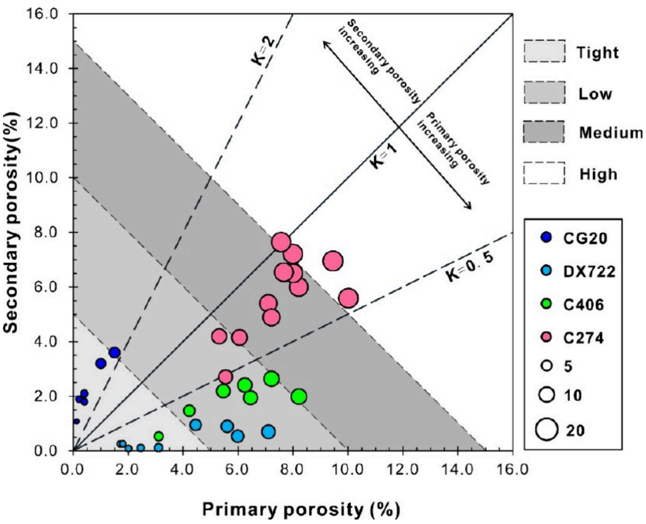

Figure 16. Bubble plots of reservoir classification based on primary, secondary, and total porosity. The "*K*" represents the ratio of secondary porosity to primary porosity. Note: The larger the diameter of the circle, the higher the porosity value.

stated, compaction causes a significant loss of the primary porosity of a reservoir, leading the reservoir to densify rapidly. However, the reservoir appeared to have a high ADR (Figure 11). How does the fluid migrated to the reservoir and promote dissolution when the reservoir is already tightly sealed? We discovered the reason for the reservoir behavior through thin section observations. Evidently, the conglomerate reservoir in Well CG20 is extensively developed with microfractures (Figure 17(a)). In the eodiagenetic and early mesodiagenetic stages, the microfractures created by compaction offer fluid migration channels, allowing organic acid to reach the reservoir.[68,69] However, the reservoir has a confined diagenetic environment with weak dissolution because of early compaction. Moreover, clay minerals, such as kaolinite, precipitated nearby produced by dissolution (Figure 17(b) and (c)), resulting in a limited increase in reservoir porosity. The widely developed microfractures significantly increased the permeability of the conglomerate reservoir in Well CG20, which may result in good seepage ability with poor pore structure of the reservoir. Nevertheless, the conglomerate reservoir of Well DX722 has few residual intergranular pores without fractures, which serve as migration pathways (Figure 17(d)). Because of the confined diagenetic environment, dissolution products are typically precipitated near the sandstone reservoirs in the depression zone.[70] Consequently, the intergranular pores are occupied by quartz overgrowth and kaolinite (Figure 17(e) and (f)). The sandstone reservoir of Well C274 in the gentle slope zone has well developed primary and secondary pores (Figure 17(g) and (h)). Its superior pore connectivity promotes the discharge of dissolution products, thereby preserving good reservoir properties. Thus, high-quality reservoirs are generally the function of a combination of primary pore retention and secondary pore generation, rather than a single contribution from secondary porosity.

6. CONCLUSIONS

Using high-resolution micro-CT, the 3D pore structures of the conglomerate and sandstone reservoirs in several secondary structural zones of the Chezhen Sag were reconstructed. The results revealed that compared with conglomerate reservoirs, sandstone reservoirs have a larger number of pores with better pore connectivity and a smaller pore volume. The shapes of sandstone pores are more regular than the shapes of conglomerate pores despite the geometry of their pores and pore throats being primarily triangular. Conglomerate reservoirs exhibit the typical features of tight reservoirs. The porosity of sandstone reservoirs is higher than that of conglomerate reservoirs, but they are more heterogeneous. The porosities of both sandstone and conglomerate reservoirs increase as their compositional maturity rises.

The reservoirs in the steep slope zone have the lowest initial porosity because of their proximity to provenance, high matrix

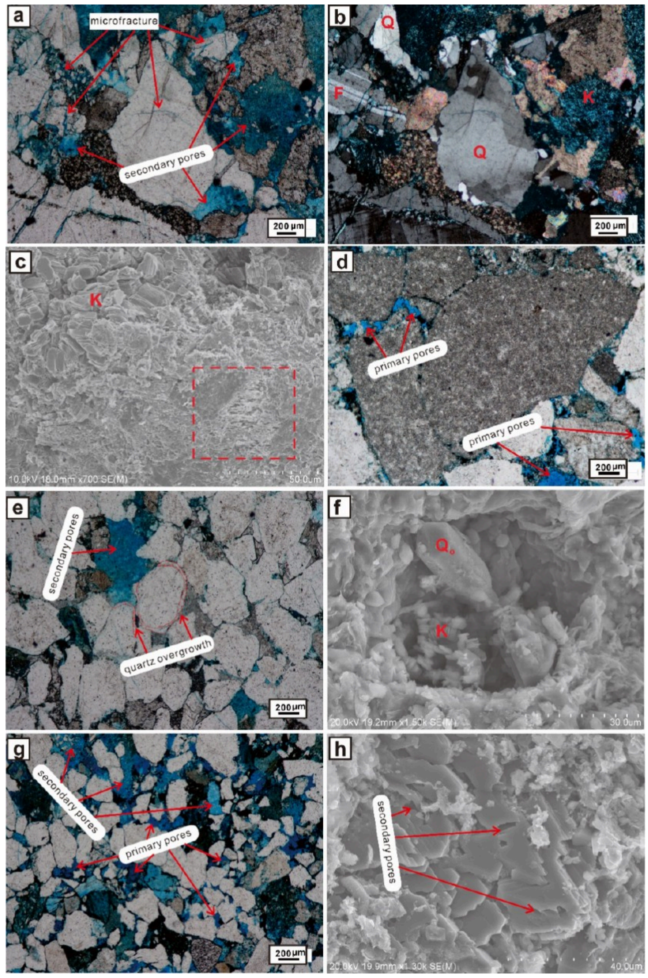

Figure 17. Optical photomicrographs and SEM images showing the petrographic features of conglomerate and sandstone reservoirs. (a) Microfractures are widely developed, and only secondary pores are visible, plane-polarized light (PPL), Well CG20, 2551.20 m. (b) Kaolinite crystals are attached to the surface of the dissolution area, cross-polarized light (CPL), Well CG20, 2551.20 m. (c) The distribution of flaky kaolinite adjacent to the dissolution area (dotted box in red), SEM, Well CG20, 2551.20 m. (d) Tight reservoir with few residual primary intergranular pores, PPL, Well DX722, 3965.5 m. (e) Quartz overgrowth develops near the dissolution pores, PPL, Well C406, 3045.10 m. (f) Authigenic quartz with hexagonal structure coexisting with kaolinite assemblages occupies the space of intergranular pores, SEM, Well C406, 3045.10 m. (g) Primary pores and secondary pores are widely developed in sandstone reservoirs in the gentle slope zone, PPL, Well C274, 2597.25 m. (h) Partially dissolved feldspar and intragranular pores, SEM, Well C274, 2597.25 m.

https://doi.org/10.1021/acsomega.4c02106
ACS Omega 2024, 9, 22952−22969

content, and poor sorting. Compaction is the key controlling factor of reservoir tightness. When it has been affected by its mineral composition, a reservoir with limited resistance to compaction will rapidly compact and almost lose its primary pores. However, some reservoirs have widely developed microfractures, which improve reservoir permeability and provide favorable conditions for dissolution. Dissolution is constrained to increase porosity because of reservoir sealing, resulting in a tight reservoir with predominant secondary pores. The loss of porosity in sandstone reservoirs in the depression zone is mainly affected by compaction and cementation, and the weak dissolution makes only a limited contribution in increasing the porosity. The sandstone reservoirs in the gentle slope zone are characterized by a high content of rigid particles with strong resistance to compaction and have a considerable number of primary pores preserved. Therefore, in an open diagenetic environment where secondary pore development is encouraged by dissolution, developing a high-quality reservoir combined primary pores with secondary pores.

In this study, a classification evaluation scheme was proposed for reservoirs based on their pore types and total porosities. By projecting the statistics of thin section identification into this plate, the reservoir quality can be quickly interpreted. By evaluating the reservoir pore type and its percentage, an insight could be gained into the evolution mechanism of porosity in clastic reservoirs.

AUTHOR INFORMATION

Corresponding Authors

Yang Li − *Cooperative Innovation Center of Unconventional Oil and Gas, Yangtze University (Ministry of Education & Hubei Province), Wuhan, Hubei 430100, PR China; Hubei Key Laboratory of Petroleum Geochemistry and Environment, Yangtze University, Wuhan 430100, PR China;* orcid.org/0000-0002-3241-4254; Email: lyugly@163.com

Yan Liu − *Hubei Key Laboratory of Petroleum Geochemistry and Environment, Yangtze University, Wuhan 430100, PR China*; Email: liuyan@yangtzeu.edu.cn

Authors

Jinlei Xiu − *Cooperative Innovation Center of Unconventional Oil and Gas, Yangtze University (Ministry of Education & Hubei Province), Wuhan, Hubei 430100, PR China; Exploration and Development Research Institute, Shengli Oilfield Company, Dongying 257000, PR China*

Yaohui Xu − *Hubei Key Laboratory of Petroleum Geochemistry and Environment, Yangtze University, Wuhan 430100, PR China*

Zhanghu Wang − *Hubei Key Laboratory of Petroleum Geochemistry and Environment, Yangtze University, Wuhan 430100, PR China*

Complete contact information is available at: https://pubs.acs.org/10.1021/acsomega.4c02106

Notes

The authors declare no competing financial interest.

ACKNOWLEDGMENTS

This study was supported by the China Postdoctoral Science Foundation (Grant No. 2021M700537), the Open Foundation of Cooperative Innovation Center of Unconventional Oil and Gas, Yangtze University (Ministry of Education & Hubei Province) (Grant No. UOG2022-11), the National Natural Science Foundation of China (Grant No. 41972122), and Natural Science Foundation of Hubei Province, China (Grant No.2022CFB642).

REFERENCES

(1) Anovitz, L. M.; Cole, D. R.; Rother, G.; Allard, L. F.; Jackson, A. J.; Littrell, K. C. Diagenetic changes in macro- to nano-scale porosity in the St. Peter Sandstone: an (ultra) small angle neutron scattering and backscattered electron imaging analysis. *Geochim. Cosmochim. Acta* **2013**, *102*, 280−305.

(2) Anovitz, L. M.; Cole, D. R.; Jackson, A. J.; Rother, G.; Littrell, K. C.; Allard, L. F.; Pollington, A. D.; Wesolowski, D. J. Effect of quartz overgrowth precipitation on the multiscale porosity of sandstone: a (U) SANS and imaging analysis. *Geochim. Cosmochim. Acta* **2015**, *158*, 199−222.

(3) Xi, K.; Cao, Y.; Haile, B. G.; Zhu, R.; Jahren, J.; Bjørlykke, K.; Zhang, X.; Hellevang, H. How does the pore-throat size control the reservoir quality and oiliness of tight sandstones? The case of the Lower Cretaceous Quantou Formation in the southern Songliao Basin, China. *Mar. Pet. Geol.* **2016**, *76*, 1−15.

(4) Li, Y.; Chang, X. C.; Yin, W.; Sun, T. T.; Song, T. T. Quantitative impact of diagenesis on reservoir quality of the Triassic Chang 6 tight oil sandstones, Zhenjing area, Ordos Basin, China. *Mar. Petrol. Geol.* **2017**, *86*, 1014−1028.

(5) Schmitt, M.; Fernandes, C. P.; Wolf, F. G.; Bellini da Cunha Neto, J. A.; Rahner, C. P.; Santiago dos Santos, V. S. Characterization of Brazilian tight gas sandstones relating permeability and angstrom-to micron-scale pore structures. *J. Nat. Gas Sci. Eng.* **2015**, *27*, 785−807.

(6) Anovitz, L. M.; Cole, D. R. Characterization and analysis of porosity and pore structures. *Rev. Mineral. Geochem.* **2015**, *80* (1), 61−164.

(7) Alyafei, N.; Mckay, T. J.; Solling, T. I. Characterization of petrophysical properties using pore-network and lattice-Boltzmann modelling: Choice of method and image sub-volume size. *J. Petrol. Sci. Eng.* **2016**, *145*, 256−265.

(8) Kate, J. M.; Gokhale, C. S. A simple method to estimate complete pore size distribution of rocks. *Eng. Geol.* **2006**, *84* (1−2), 48−69.

(9) Gao, H.; Li, H. A. Pore structure characterization, permeability evaluation and enhanced gas recovery techniques of tight gas sandstones. *J. Nat. Gas Sci. Eng.* **2016**, *28*, 536−547.

(10) Geiger, J.; Hunyadfalvi, Z.; Bogner, P. Analysis of small-scale heterogeneity in clastic rocks by using computerized X-ray tomography (CT). *Eng. Geol.* **2009**, *103* (3−4), 112−118.

(11) Li, Y.; Chang, X.; Yin, W.; Wang, G. W.; Zhang, J. L.; Shi, B. B.; Zhang, J. H.; Mao, L. X. Quantitative identification of diagenetic facies and controls on reservoir quality for tight sandstones: a case study of the Triassic Chang 9 oil layer, Zhenjing area, Ordos Basin. *Mar. Petrol. Geol.* **2019**, *102*, 680−694.

(12) Zhang, F.; Jiang, Z.; Sun, W.; Li, Y.; Zhang, X.; Zhu, L.; Wen, M. A multiscale comprehensive study on pore structure of tight sandstone reservoir realized by nuclear magnetic resonance, high pressure mercury injection and constant-rate mercury injection penetration test. *Mar. Pet. Geol.* **2019**, *109*, 208−222.

(13) Tian, W.; Lu, S.; Zhang, J.; Gao, Y.; Huang, W.; Wen, Z.; Li, J.; Li, J. NMR characterization of fluid mobility in low-permeability conglomerates: An experimental investigation of spontaneous imbibition and flooding. *J. Pet. Sci. Eng.* **2022**, *214*, 110483.

(14) Yao, Y.; Liu, D.; Che, Y.; Tang, D.; Tang, S.; Huang, W. Non-destructive characterization of coal samples from China using microfocus X-ray computed tomography. *Int. J. Coal Geol.* **2009**, *80* (2), 113−123.

(15) Vergés, E.; Tost, D.; Ayala, D.; Ramos, E.; Grau, S. 3D pore analysis of sedimentary rocks. *Sediment. Geol.* **2011**, *234* (1−4), 109−115.

(16) BAI, B.; ZHU, R.; WU, S.; YANG, W.; Gelb, J.; Gu, A.; ZHANG, X.; SU, L. Multi-scale method of nano(micro)-CT study on microscopic pore structure of tight sandstone of Yanchang formation, Ordos basin. *Pet. Explor. Dev.* **2013**, *40* (3), 354.

(17) Saxena, N.; Hofmann, R.; Alpak, F. O.; Dietderich, J.; Hunter, S.; Day-Stirrat, R. J. Effect of image segmentation & voxel size on micro-CT computed effective transport & elastic properties. *Mar. Pet. Geol.* **2017**, *86*, 972−990.

(18) Munawar, M. J.; Lin, C.; Cnudde, V.; Bultreys, T.; Dong, C.; Zhang, X.; De Boever, W.; Zahid, M. A.; Wu, Y. Petrographic characterization to build an accurate rock model using micro-CT: Case study on low-permeable to tight turbidite sandstone from Eocene Shahejie Formation. *Micron* **2018**, *109*, 22−33.

(19) Tiwari, P.; Deo, M.; Lin, C. L.; Miller, J. D. Characterization of oil shale pore structure before and after pyrolysis by using X-ray micro CT. *Fuel* **2013**, *107*, 547−554.

(20) Cnudde, V.; Boone, M. N. High-resolution X-ray computed tomography in geosciences: A review of the current technology and applications. *Earth-Sci. Rev.* **2013**, *123*, 1−17.

(21) Mayo, S.; Josh, M.; Nesterets, Y.; Esteban, L.; Pervukhina, M.; Clennell, M. B.; Maksimenko, A.; Hall, C. Quantitative micro-porosity characterization using synchrotron micro-CT and xenon K-edge subtraction in sandstones, carbonates, shales and coal. *Fuel* **2015**, *154*, 167−173.

(22) Lai, J.; Wang, G.; Wang, Z.; Chen, J.; Pang, X.; Wang, S.; Zhou, Z.; He, Z.; Qin, Z.; Fan, X. A review on pore structure characterization in tight sandstones. *Earth-Sci. Rev.* **2018**, *177*, 436−457.

(23) Liu, L. L.; Li, Y.; Dong, H. Z.; Sun, Z. Q. Diagenesis and reservoir quality of paleocene tight sandstones, Lishui sag, east China Sea Shelf basin. *J. Petrol. Sci. Eng.* **2020**, *195*, 107615.

(24) Yu, B.; Fan, W.; Fan, J. H.; Dijkstra, T. A.; Wei, Y. N.; Wei, T. T. X-ray micro-computed tomography (μ-CT) for 3D characterization of particle kinematics representing water-induced loess microfabric collapse. *Eng. Geol.* **2020**, *279*, 105895.

(25) Sun, X.; Li, X.; Zheng, B.; He, J.; Mao, T. Study on the progressive fracturing in soil and rock mixture under uniaxial compression conditions by CT scanning. *Eng. Geol.* **2020**, *279*, 105884.

(26) Aghaei, A.; Piri, M. Direct pore-to-core up-scaling of displacement processes: Dynamic pore network modeling and experimentation. *J. Hydrol.* **2015**, *522*, 488−509.

(27) Zhang, P.; Lee, Y. I.; Zhang, J. A review of high-resolution X-ray computed tomography applied to petroleum geology and a case study. *Micron* **2019**, *124*, 102702.

(28) Ishii, E.; Sanada, H.; Iwatsuki, T.; Sugita, Y.; Kurikami, H. Mechanical strength of the transition zone at the boundary between opal-A and opal-CT zones in siliceous rocks. *Eng. Geol.* **2011**, *122* (3−4), 215−221.

(29) Christe, P.; Turberg, P.; Labiouse, V.; Meuli, R.; Parriaux, A. An X-ray computed tomography-based index to characterize the quality of cataclastic carbonate rock samples. *Eng. Geol.* **2011**, *117* (3−4), 180−188.

(30) Desbois, G.; Urai, J. L.; Kukla, P. A.; Konstanty, J.; Baerle, C. High-resolution 3D fabric and porosity model in a tight gas sandstone reservoir: A new approach to investigate microstructures from mm-to nm-scale combining argon beam cross-sectioning and SEM imaging. *J. Petrol. Sci. Eng.* **2011**, *78* (2), 243−257.

(31) Fusi, N.; Martinez-Martinez, J. Mercury porosimetry as a tool for improving quality of micro-CT images in low porosity carbonate rocks. *Eng. Geol.* **2013**, *166*, 272−282.

(32) Liu, X.; Wang, J.; Ge, L.; Hu, F.; Li, C.; Li, X.; Yu, J.; Xu, H.; Lu, S.; Xue, Q. Pore-scale characterization of tight sandstone in Yanchang Formation Ordos Basin China using micro-CT and SEM imaging from nm-to cm-scale. *Fuel* **2017**, *209*, 254−264.

(33) Cao, Y. C.; Wang, Y. Z.; Gluyas, J. G.; Liu, H. M.; Liu, H. M.; Song, M. S. Depositional model for lacustrine nearshore subaqueous fans in a rift basin: the Eocene Shahejie Formation, dongying sag, Bohai Bay Basin, China. *Sedimentology* **2018**, *65*, 2117−2148.

(34) Wang, Y. Z.; Mao, C. Diagenesis of the Cretaceous glutenite and its control on the reservoir porosity in the Fangzheng depression, Northeast China. *Environ. Earth Sci.* **2020**, *79*, 1−8.

(35) Tian, W.; Lu, S.; Huang, W.; Wang, W.; Li, J.; Gao, Y.; Zhan, Z.; Sun, Y. Quantifying the control of pore types on fluid mobility in low-permeability conglomerates by integrating various experiments. *Fuel* **2020**, *275*, 117835.

(36) Li, C.; Zhang, L. K.; Luo, X. R.; Lei, Y. H.; Yu, L.; Cheng, M.; Wang, Y. S.; Wang, Z. L. Overpressure generation by disequilibrium compaction or hydrocarbon generation in the Paleocene Shahejie Formation in the Chezhen Depression: insights from logging responses and basin modeling. *Mar. Petrol. Geol.* **2021**, *133*, 105258.

(37) Rui, Z.; Guo, T.; Feng, Q.; Qu, Z.; Qi, N.; Gong, F. Influence of gravel on the propagation pattern of hydraulic fracture in the glutenite reservoir. *J. Petrol. Sci. Eng.* **2018**, *165*, 627−639.

(38) Zhu, X. M.; Zhao, D. N.; Jiang, S. X.; Ge, J. W.; Zhang, S. P.; Han, X. F.; Liu, X. Digenetic sequence of low porosity and permeability reservoirs from nearshore subaqeous fan of Shahejie formation in the steep slope zone of Chezhen depression, Bohai Bay Basin. *J. Earth Sci. Environ.* **2014**, *36*, 1−9. (in Chinese with English abstract).

(39) Yang, T.; Cao, Y. C.; Friis, H.; Liu, K. Y.; Wang, Y. Z.; Zhou, L. L.; Yuan, G. H.; Xi, K. L.; Zhang, S. M. Diagenesis and reservoir quality of lacustrine deep-water gravityflow sandstones in the Eocene Shahejie Formation in the Dongying sag, Jiyang depression, eastern China. *AAPG Bull.* **2020**, *104*, 1045−1073.

(40) Song, M. S.; Li, Y. Q. Evaluation and practice of fine petroleum exploration in the Jiyang depression. *China Petrol. Explor.* **2020**, *25*, 93−101. (in Chinese with English abstract).

(41) Li, Y.; Zhang, J.; Xu, Y.; Chen, T.; Yan, X.; Sun, L.; Tian, W. Genetic mechanism and grading assessment of the glutenite reservoirs in the Eocene Shahejie Formation, Chezhen Sag, Bohai Bay Basin. *J. Petrol. Sci. Eng.* **2022**, *211*, 110226.

(42) Feng, C.; Lei, D.; Qu, J.; Huo, J. Controls of paleo-overpressure, faults and sedimentary facies on the distribution of the high pressure and high production oil pools in the lower Triassic Baikouquan Formation of the Mahu Sag, Junggar Basin, China. *J. Petrol. Sci. Eng.* **2019**, *176*, 232−248.

(43) Otsu, N. A threshold selection method from gray-level histogram. *IEEE Trans. Syst.Man Cybern.* **1979**, *9* (1), 62−66.

(44) Mason, G.; Morrow, N. R. Capillary behavior of a perfectly wetting liquid in irregular triangular tubes. *J. Colloid Interface Sci.* **1991**, *141* (1), 262−274.

(45) Giesche, H. Mercury porosimetry: a general (practical) overview. *Part. Part. Syst. Charact.* **2006**, *23* (1), 9−19.

(46) Dong, H.; Blunt, M. J. Pore-network extraction from micro-computerized-tomography images. *Phys. Rev. E* **2009**, *80* (3), 036307.

(47) Andrew, M.; Bijeljic, B.; Blunt, M. J. Pore by pore capillary pressure measurements using X ray microtomography at reservoir conditions: Curvature, snap off, and remobilization of residual CO2. *Water Resour. Res.* **2014**, *50* (11), 8760−8774.

(48) Sun, Z.; Torres Verdín, C. The Role of Pore Shape and Pore Space Heterogeneity in Non Archie Behavior of Resistivity Index Curves. *J. Geophys. Res.: Solid Earth* **2022**, *127*, JB024792.

(49) Cui, R.; Hassanizadeh, S. M.; Sun, S. Pore-network modeling of flow in shale nanopores: Network structure, flow principles, and computational algorithms. *Earth-Sci. Rev.* **2022**, *234*, 104203.

(50) Lindquist, W. B.; Venkatarangan, A.; Dunsmuir, J.; Wong, T. F. Pore and throat size distributions measured from synchrotron X ray tomographic images of Fontainebleau sandstones. *J. Geophys. Res.: Solid Earth* **2000**, *105* (B9), 21509−21527.

(51) Bernabé, Y.; Li, M.; Maineult, A. Permeability and pore connectivity: a new model based on network simulations. *J. Geophys. Res.: Solid Earth* **2010**, DOI: 10.1029/2010JB007444.

(52) Raoof, A.; Hassanizadeh, S. M. A new method for generating pore-network models of porous media. *Transp. Porous Media* **2010**, *81* (3), 391−407.

(53) Sahimi, M. *Flow and transport in porous media and fractured rock: from classical methods to modern approaches*; John Wiley & Sons, 2011.
(54) Rabbani, A.; Ayatollahi, S.; Kharrat, R.; Dashti, N. Estimation of 3-D pore network coordination number of rocks from watershed segmentation of a single 2-D image. *Adv. Water Resour.* **2016**, *94*, 264−277.
(55) Beard, D. C.; Weyl, P. K. Influence of texture on porosity and permeability of unconsolidated sand. *AAPG Bull.* **1973**, *57* (2), 349−369.
(56) Scherer, M. Parameters influencing porosity in sandstones: a model for sandstone porosity prediction. *AAPG Bull.* **1987**, *71*, 485−491.
(57) Ramm, M. Reservoir quality and its relationship to facies and provenance in middle to upper jurassic sequences, northeastern North Sea. *Clay Miner.* **2000**, *35*, 77−94.
(58) Bjørlykke, K. Relationships between depositional environments, burial history and rock property, some principal aspects of diagenetic process in sedimentary basins. *Sediment. Geol.* **2014**, *301*, 1−14.
(59) Morad, S.; Al-Ramadan, K.; Ketzer, J. M.; De Ros, L. F. The impact of diagenesis on the heterogeneity of sandstone reservoirs: a review of the role of depositional fades and sequence stratigraphy. *AAPG Bull.* **2010**, *94*, 1267−1309.
(60) Taylor, T. R.; Giles, M. R.; Hathon, L. A.; Diggs, T. N.; Braunsdorf, N. R.; Birbiglia, G. V.; Kittridge, M. G.; Macaulay, C. I.; Espejo, I. S. Sandstone diagenesis and reservoir quality prediction: models, myths, and reality. *AAPG Bull.* **2010**, *94*, 1093−1132.
(61) Giles, M.R.; de Boer, R.B. Origin and significance of redistributional secondary porosity. *Mar. Petrol. Geol.* **1990**, *7*, 378−397.
(62) Higgs, K. E.; Zwingmann, H.; Reyes, A. G.; Funnell, R. H. Diagenesis, porosity evolution, and petroleum emplacement in tight gas reservoirs, Taranaki Basin, New Zealand. *J. Sediment. Res.* **2007**, *77* (12), 1003−1025.
(63) Bjørlykke, K.; Jahren, J. Open or closed geochemical systems during diagenesis in sedimentary basins: constraints on mass transfer during diagenesis and the prediction of porosity in sandstone and carbonate reservoirs. *AAPG Bull.* **2012**, *96*, 2193−2214.
(64) Lai, J.; Wang, G. W.; Huang, L. X.; Guan, B.; Jiang, C.; Ran, Y.; Wang, D. Quantitative classification and logging identification method for diagenetic facies of tight sandstones. *Bulletin of mineralogy, Petrology and Geochemistry (in Chinese with English abstract)* **2015**, *34* (1), 128−138.
(65) Yuan, G.; Cao, Y.; Gluyas, J.; Li, X.; Xi, K.; Wang, Y.; Jia, Z.; Sun, P.; Oxtoby, N. H. Feldspar dissolution, authigenic clays, and quartz cements in open and closed sandstone geochemical systems during diagenesis: Typical examples from two sags in Bohai Bay Basin, East China. *AAPG Bull.* **2015**, *99* (11), 2121−2154.
(66) Soeder, D. J.; Chowdiah, P. Pore geometry in high and low-permeability sandstones, Travis Peak Formation, east Texas. *SPE Form. Eval.* **1990**, *5* (4), 421−430.
(67) Nelson, P. H. Pore-throat sizes in sandstones, tight sandstones, and shales. *AAPG Bull.* **2009**, *93* (3), 329−340.
(68) Grude, S.; Dvorkin, J.; Landrø, M. Permeability variation with porosity, pore space geometry, and cement type: a case history from the Snøhvit field, the Barents sea. *Geophysics* **2015**, *80* (1), D43−D49.
(69) Kassab, M. A.; Abu Hashish, M. F.; Nabawy, B. S.; Elnaggar, O. M. Effect of kaolinite as a key factor controlling the petrophysical properties of the Nubia sandstone in central Eastern desert, Egypt. *J. Afr. Earth Sci.* **2017**, *125*, 103−117.
(70) Yuan, G.; Cao, Y.; Gluyas, J.; Jia, Z. Reactive transport modeling of coupled feldspar dissolution and secondary mineral precipitation and its implication for diagenetic interaction in sandstones. *Geochim. Cosmochim. Acta* **2017**, *207*, 232−255.

https://doi.org/10.1021/acsomega.4c02106
ACS Omega 2024, 9, 22952−22969